IHEP-CEPC-DR-2018-XX

IHEP-EP-2018-XX

IHEP-TH-2018-XX

CEPC

Conceptual Design Report

Volume II - Physics & Detector

The CEPC Study Group

March 2018

ACKNOWLEDGMENTS

The CEPC-SPPC Conceptual Design Report (CDR) was prepared and written by the CEPC Study Group. The study was organised and led by scientists from the Institute of High Energy Physics (IHEP) of the Chinese Academy of Sciences (CAS), and from many universities and other institutes in China and abroad. The study was partially supported ...

...

CONTENTS

CHAPTER 1

EXPERIMENTAL CONDITIONS AND DETECTOR CONCEPTS

1.1 Experimental conditions

The CEPC can be operated as a Z factory ($\sqrt{s}$ = 91.2 GeV) and a Higgs factory ($\sqrt{s}$ = 240 GeV). It could also perform W threshold scan at $\sqrt{s}$ around 160 GeV and determines precisely the mass and width of the W boson. According to the CEPC Accelerator CDR [**?**], the luminosities at these center of mass energies are listed in Table 1.1.

As an electron positron collider, the CEPC is an extremely clean machine. Fig. 1.1 shows the cross section of leading SM processes at the electron positron collision. The ratio between the cross sections of the Higgs signal and the inclusive physics events is roughly $10^{-2} \sim 10^{-3}$ at CEPC [**?**], eight orders of magnitudes larger than that in the LHC [**?**]. At the CEPC, the entire physics event rate is so low that every physics event can be recorded, providing ideal samples for the precision measurements.

The beam parameters of different CEPC physics operations are summarized in Tab **??**. The main physics objective and leading physics requirements for the detector/collider system is discussed below.

1.1.1 Higgs Operation

The CEPC Higgs operation is expected to accumulate an integrated luminosity of $5\ ab^{-1}$ and produce 1 million Higgs boson. Its main physics objective is to determine precisely the Higgs boson properties. The Higgs signal event rate is roughly of the order of 0.01 Hz: roughly 1 Higgs boson every two minutes.

The typical measurements including the absolute measurement of $\sigma(ZH)$ via the recoil mass method, the Higgs event rates measurements, and the differential measurements on the Higgs events.

Operation mode	Z factory	W threshold scan	Higgs factory
$\sqrt{s}$/GeV	91.2	158 - 172	240
$\mathrm{L}/10^{34}\mathrm{cm}^{-2}\mathrm{s}^{-1}$	16-32	10	3
Running time/year	2	1	7
Integrated Luminosity/ab^{-1}	8 - 16	2.5	5
Higgs yield	-	-	10^6
W yield	-	10^7	10^8
Z yield	10^{11-12}	10^9	10^9

Table 1.1: Instance luminosity at different $\sqrt{s}$ and anticipated boson yields at the CEPC.

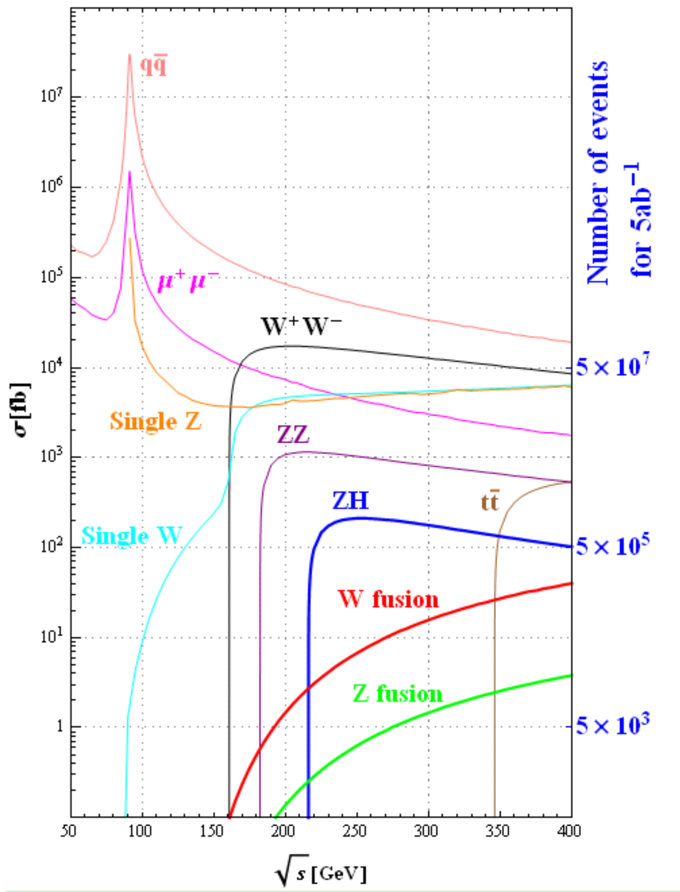

Figure 1.1: Cross sections of the leading Standard Model processes at non polarized electron positron collision (Left) and at proton collision (Right)

	Higgs	*W*	*Z (3T)*	*Z (2T)*
Number of IPs	2			
Beam energy (GeV)	120	80	45.5	
Circumference (km)	100			
Synchrotron radiation loss/turn (GeV)	1.73	0.34	0.036	
Crossing angle at IP (mrad)	16.5×2			
Piwinski angle	2.58	7.0	23.8	
Number of particles/bunch N_e (10^{10})	15.0	12.0	8.0	
Bunch number	242	1524	12000 (10% gap)	
Bunch spacing (ns)	680	210	25	
Beam current (mA)	17.4	87.9	461.0	
Synchrotron radiation power (MW)	30	30	16.5	
Bending radius (km)	10.7			
Momentum compaction (10^{-5})	1.11			
β function at IP β_x^* / β_y^* (m)	0.36/0.0015	0.36/0.0015	0.2/0.0015	0.2/0.001
Emittance x/y (nm)	1.21/0.0031	0.54/0.0016	0.18/0.004	0.18/0.0016
Beam size at IP σ_x/σ_y (μm)	20.9/0.068	13.9/0.049	6.0/0.078	6.0/0.04
Beam-beam parameters ξ_x/ξ_y	0.031/0.109	0.013/0.106	0.004/0.056	0.004/0.072
RF voltage V_{RF} (GV)	2.17	0.47	0.10	
RF frequency f_{RF} (MHz)	650			
Harmonic number	216816			
Natural bunch length σ_z (mm)	2.72	2.98	2.42	
Bunch length σ_z (mm)	3.26	5.9	8.5	
Damping time $\tau_x/\tau_y/\tau_E$ (ms)	46.5/46.5/23.5	156.4/156.4/ 74.5	849.5/849.5/425.0	
Natural Chromaticity	-493/-1544	-493/-1544	-520/-1544	-520/-3067
Betatron tune ν_x/ν_y	363.10 / 365.22			
Synchrotron tune ν_s	0.065	0.0395	0.028	
HOM power/cavity(2cell) (kw)	0.54	0.75	1.94	
Natural energy spread (%)	0.1	0.066	0.038	
Energy acceptance requirement (%)	1.35	0.40	0.23	
Energy acceptance by RF (%)	2.06	1.47	1.70	
Photon number due to beamstrahlung	0.29	0.35	0.55	
Lifetime _simulation (min)	100			
Lifetime (hour)	0.67	1.4	4.0	2.1
F (hour glass)	0.89	0.94	0.99	
Luminosity/IP *L* ($10^{34}cm^{-2}s^{-1}$)	3	10	17	32

Figure 1.2: Main beam parameters for the CEPC operation

Combing these measurements leads to a model-independent determination of the Higgs boson decay branching ratio, the couplings between the Higgs boson and its decay final states, and the total Higgs width. These quantities could typically be determined to a relative precision of 0.1% - 1%, one order of magnitude better than the HL-LHC experiments. The differential measurements provides important input for the quantum number determination and the coefficient measurements within the Effective Lagrangian Theory framework. In addition, the recoil mass method and the clean collision environments make CEPC an extremely sensitive probe to the Higgs exotic decays. A general exploration shows that the 95% C.L. of the Higgs exotic decays could be limited to the range of per mille level to 10^{-6} [**?**]. On top of the Higgs events, roughly 100 million W bosons and 1 billion Z bosons will be generated. These events could be used for both EW precision measurements and in-situ calibration for the detector.

For the Higgs measurement, the integrated luminosity should be measured to an relative accuracy better than 0.1%. To limit the uncertainty on the Higgs mass measurement via the recoil mass spectrum, the beam energy need to be calibrated to an accuracy of 1 MeV.

1.1.2 Z pole Operation

The total statistic of the Z pole statistics would be 5 orders of magnitude higher than that of the LEP. In fact, the CEPC could produce the entire LEP I data sample in 5 minutes. From which, electroweak observables such as $A_{FB}^{0,b}$, R_b, and those measured with the Z line shape can be determined. In addition, the Z pole data also provide huge good access for the flavor physics.

At 91.2 GeV center of mass energy, the leading physics process is the $Z \rightarrow fermion$ events, plus a small fraction of the $\gamma\gamma$ background and the Bhabha events. These events have so clean signature that it's easy to distinguish them from each other. However, giving the extremely small statistic uncertainty, the understanding and calibration of the mis-identifications between different physics events are essential.

Being the weak interaction mediator, the Z boson decays into all kinds of the SM fermions except the top quark. In order to distinguish different Z boson decay modes, an high efficiency, high purity identification of leptons, taus, and jets, are highly appreciated. The precise energy-momentum reconstruction, especially the good angular resolution for these physics objects, are crucial for the Z pole physics measurements such as A_{FB}^{μ} and the weak mixing angle. To determine precisely the measurements associated with the b-jets, a precise reconstruction of jet flavor and jet charge is crucial.

In order to extract precisely the Z line shape information, the beam energy need to be calibrated to an accuracy better than MeV, and the luminosity is required to be controlled to a relative accuracy of 10^{-4}.

The CEPC Z pole operation provides a large statistic of $Z \rightarrow \tau^+\tau^-$ sample. Many photons are generated in the π^0s from the τ decay and it's crucial to identify these individual photons. In other word, the CEPC detector should provides good separation performance and count precisely how many photons (π^0s) are generated in the $Z \rightarrow \tau^+\tau^-$ events. As for the flavor physics measurement, the identification of the charged kaon is essential.

The Z line shape scan makes stringent requirement on the luminosity measurements. Typically, the luminosity need to be measured to a relative accuracy of 10^{-4}. The beam energy need to be calibrated to an accuracy of 100 keV.

In order to deliver ... The number of bunches in the Z pole

1.1.3 W threshold scan

At the W threshold scan, the CEPC could produce 10^7 W event in a year. The W threshold scan is mainly devoting to the W boson mass and W boson width measurements. In addition, it provides essential input for the TGC measurements.

A precise determination of the beam energy is indispensable for the W threshold scan. Typically, the beam energy need to be calibrated to sub-MeV level accuracy.

It need to be reminded that the EW and the Higgs measurements provide complementary information, and a combination significantly enhances the physics reach [**?**] [**?**]. The dedicated physics requirements for the CEPC physics program are summarized below.

1.2 Physics Requirements

As a tremendous Higgs, Z, and W boson factory, the CEPC should be equipped with detectors that can identify all the corresponding physics objects with high efficiency, high purity and to measure them with high precision. In addition, the CEPC physics program requires a precise determination of the instant luminosity, a precise control and monitoring of the beam energy. Generally, the CEPC detector is required to:

1, Be adequate to the CEPC collision environment: the detector should be fast enough to record all the physics events and robust enough against the irradiation.

2, Highly hermetic. The detector should provide a solid angle coverage of $|cos(\theta)| < 0.99$.

3, The luminosity should be measured to a relative accuracy of 0.1% for the Higgs operation, and 10^{-4} for the Z line shape scan.

4, The beam energy should be measured to an accuracy of the order of 1 MeV for the Higgs operation, and 100 keV for the Z pole and W mass threshold scan.

The detailed requirements on the physics objects are discussed below:

1.2.1 Multiplicity

The final state particles could be classified into charged particles, photons, and the neutral hadrons. Corresponding to the leading SM processes at the CEPC Higgs operation (the WW, ZZ, and ZH process), the multiplicities are shown in Fig. 1.3. The photons and the charged tracks follows a similar distribution, which is significantly higher than that for the neutral hadrons. In fact, the charged tracks and the photons carry most of the jet energy.

The multiplicity of photons and charged tracks could be as high as 100. Meanwhile, lots of final state particles have very small angles in between, as most of the tracks and photons are produced in jets. In other word, especially under the context of Particle Flow algorithm, it's essential to separate efficiently those final state particles.

1.2.2 Tracking

The CEPC detector should have excellent track finding efficiency and track momentum resolution. Corresponding to the leading SM processes at the CEPC Higgs operation

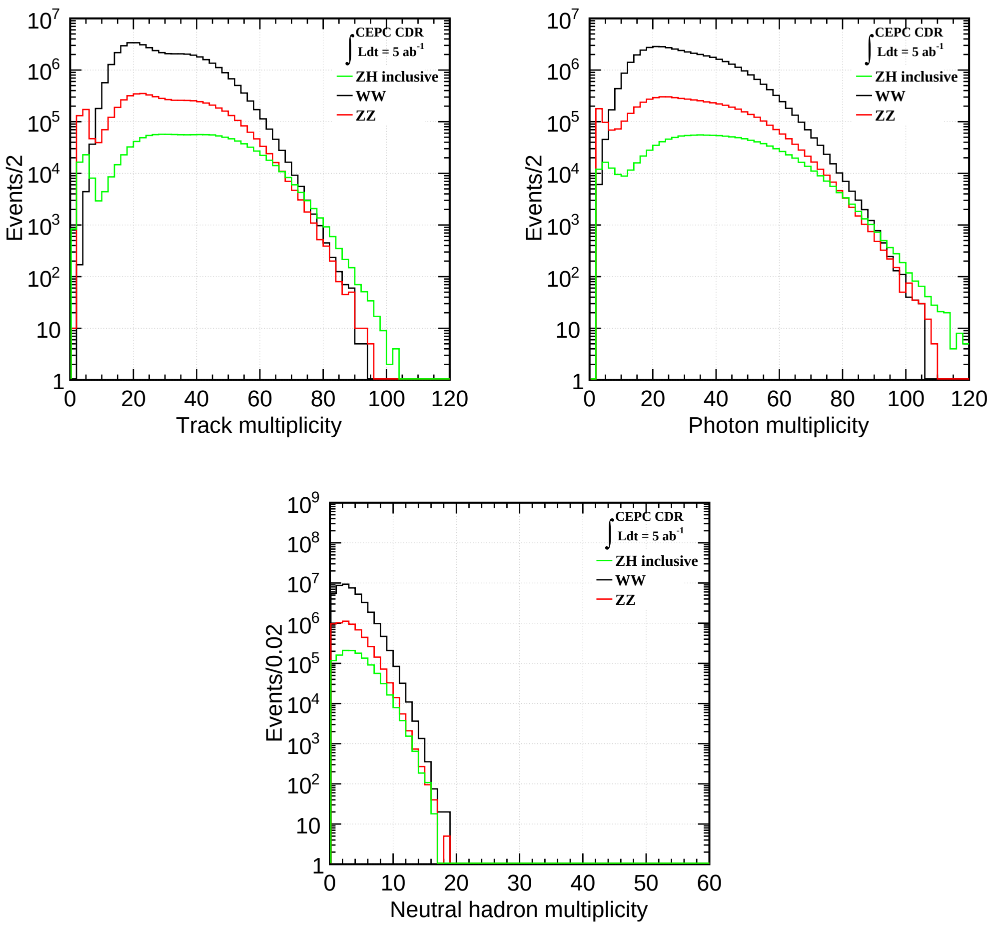

Figure 1.3: The multiplicity of charged particle, photons, and neutral hadrons at the leading physics processes at the CEPC Higgs operation.

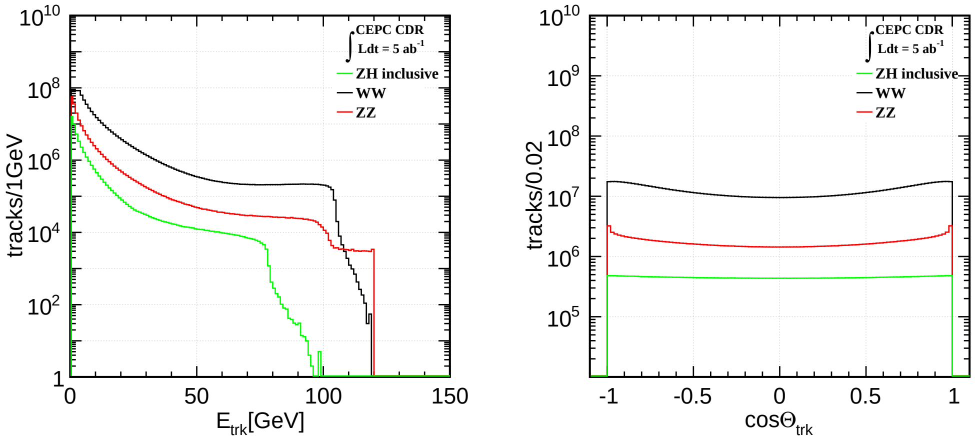

Figure 1.4: Energy and polar angle distribution of charged particles at the leading physics processes at the CEPC Higgs operation.

(the WW, ZZ, and ZH process), the energy and polar angle distributions of the charged particles are shown in Fig. 1.4. These distributions are normalized to 5 ab^{-1}, the nominal luminosity at the CEPC.

In terms of the polar angle distribution, the ZH process is almost flat in the polar angle direction, while the other two processes are more forward region oriented. In other word, the detector is required to have a full solid angle coverage.

In the energy distribution, these three processes shares the same pattern. For energy below 20 GeV, these distributions follow an exponential distribution, while in the high energy side there is a flat plateau with a steep cliff. Therefore, the CEPC detector is required to have a high efficiency track reconstruction, especially for these low energy tracks. Meanwhile, it should maintain an excellent momentum resolution and linearity for a wide energy range (0.1 GeV - 120). For any tracks within the detector acceptance and an transverse momentum larger than 1 GeV, we request an track finding efficiency better than 99%. The momentum resolution is required to achieve a relative accuracy at per mille level, in order to measure the $H \to \mu^+\mu^-$ signal and to reconstruct precisely the Higgs boson mass from the recoil mass distribution at l^+l^-H events.

1.2.3 Lepton

The classification of different physics event highly relies on the lepton information. It other word, the lepton is one of the most important physics signature.

At the CEPC Higgs opearation, roughly 7% of the Higgs bosons are generated with a pair of leptons. These l^+l^-H samples are the golden signal for the Higgs recoil mass analysis. Fig. 1.5 shows the energy and angular distribution of the leptons, where the prompt leptons and these generated in Higgs decay cascade are separated. The prompt muons at the $\mu^+\mu^-H$ events has a flat distribution within the kinematic allowance: from 20 - 100 GeV. The prompt muon energy distribution has a low energy tail, induced by the Final State Radiation effect (FSR). The prompt electron-positron at the e^+e^-H events follows a similar pattern, except the population increases at energy smaller than 10 GeV. These low-energy prompt electron-positrons are mainly induced by the Z fusion events.

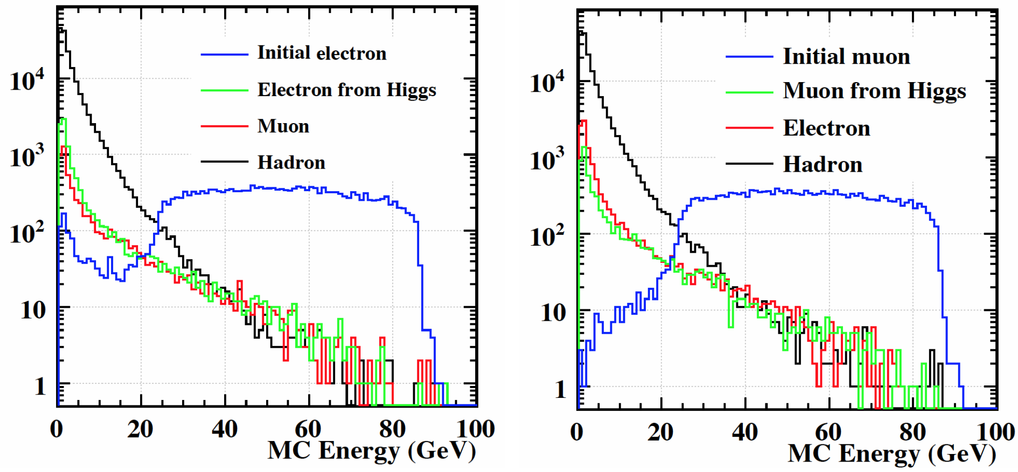

Figure 1.5: Energy spectrum of the leptons and the charged hardons in the e^+e^-H events (left) and the $\mu^+\mu^-H$ events (right).

The Higgs decay also generates leptons, which is mostly concentrated in the low energy side, but can have energies as high as 70 GeV. These high energy leptons are mainly generated from $H \rightarrow \tau^+ tau^-, ZZ^*, WW^*$ decay cascades.

In order to reconstruct all the prompt leptons, an excellent lepton identification performance for isolated leptons with energy higher than 5 GeV, is regarded as a must for the CEPC detector design. Meanwhile, the low energy leptons are numerous in the Higgs decay cascade, and a good lepton identification performance for these low energy leptons are highly appreciated.

1.2.4 Particle identification

The particle identification, especially the identification of charged kaons, is crucial for the flavor physics. In addition, the kaon identification is highly appreciated for the jet flavor tagging and jet charge reconstruction. Typically, we request the efficiency and purity of the kaon identification at the inclusive Z pole sample to be better than 90%.

1.2.5 Photons

The photons is crucial for the jet energy resolution, the $H \rightarrow \gamma\gamma$ branching ratio measurements, and the physics with τ final states. Fig. 1.7 shows the energy and polar angle distribution for the inclusive photons, and the ISR photons, from these benchmark physics processes at the CEPC Higgs operation.

As for the photon reconstruction, we request a photon identification efficiency higher than 99% and a misidentification rate smaller than 5%, for non-converted, isolated photons with energy higher than 1 GeV. In terms of the photon energy resolution, it should secures a relative mass resolution at $H \rightarrow \gamma\gamma$ final state better than 3%. In addition, the photons generated from π^0 decays, either from the τ decay cascade or from the jet fragmentations, should be clearly separated.

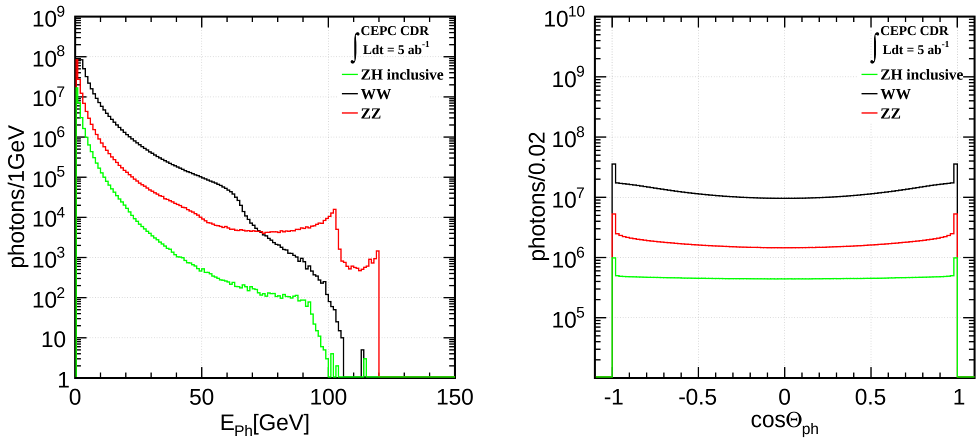

Figure 1.6: Energy and polar angle distribution of all photons at the leading physics processes at the CEPC Higgs operation.

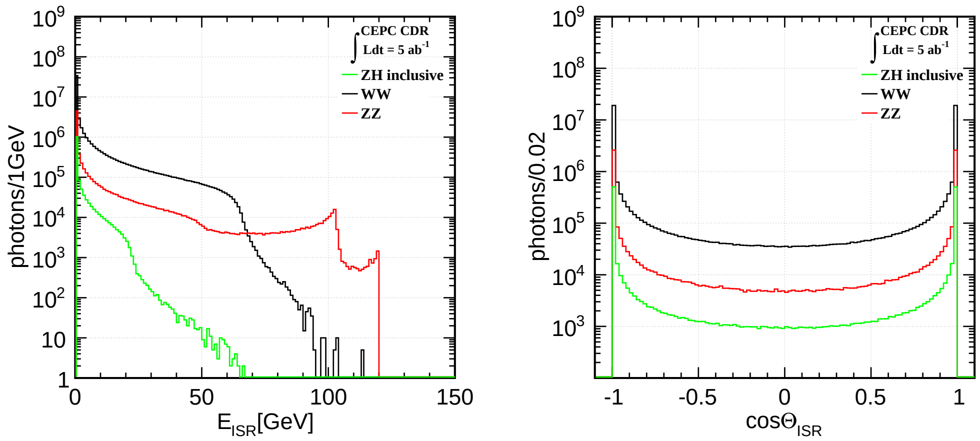

Figure 1.7: Energy and polar angle distribution of ISR photons from the leading physics processes at the CEPC Higgs operation.

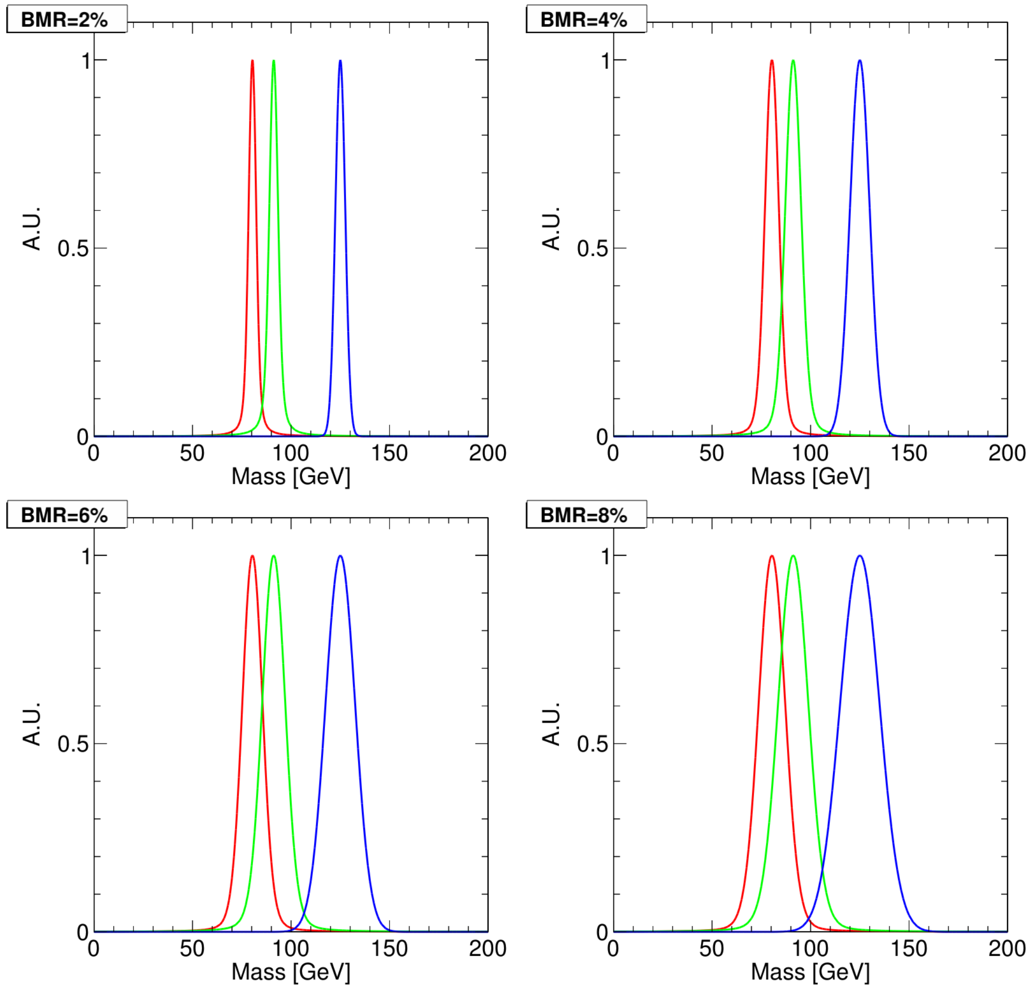

Figure 1.8: Invariant mass distribution of H, W, and Z bosons at different boson mass resolution.

1.2.6 Jets and Missing energy

The jet reconstruction is essential for the CEPC physics program, since the majority of W, Z, and Higgs bosons decays into hadronic final states. At the Particle Flow oriented design, the jet is constructed via clustering algorithms from the final state particles. Therefore, the jet reconstruction is determined by the reconstruction of final state particle, and the jet clustering algorithm. Consequently, the jet reconstruction performance should be evaluated at two stages.

The first is the boson mass resolution for massive SM bosons. The boson mass resolution represents the jet energy resolution with perfect jet clustering, or more accurately, a perfect identification of the color singlet. A good boson mass resolution is a pre-request for the distinguish of WW, ZZ, and ZH events decay into 4 jets final states, and to distinguish $H \to WW^*, ZZ^* \to 4jets$ from each other. In order to distinguish the W, Z, and the Higgs boson from their hadronic decay final state, a boson mass resolution better than 4% is required.

The missing energy measurement with jet final states is also determined by the boson mass resolution. The physics benchmark for the missing energy-momentum measurement

Figure 1.9: Recoil mass distribution of qqH, H->invisible events with $ZZ \rightarrow qqvv$ backgrounds at different boson mass resolution.

is the $Br(H \rightarrow invisible)$ measurement with qqH final states. For this benchmark, a boson mass resolution better than 4% is certainly appreciated.

The identification of individual jet, and its energy-momentum reconstruction is crucial for the CEPC physics measurements. The individual jet energy response is highly depending on the event topology and the jet clustering algorithms. A detailed analyses is required to disentangle the actual physics requirement, which need to be analyzed profoundly.

1.2.7 Flavor Tagging

One of the key physics objective of the CEPC Higgs program is the determination of $g(Hcc)$. The CEPC detector system is therefore required to efficiently distinguish the b-jets, the c-jets, and the light jets from each other. A decent flavor tagging performance is also highly appreciated in EW precision measurements.

The classification of different kinds of jets mainly relies on the reconstruction of secondary vertex, where the performance of the vertex system is crucial. The clean collision environment of the CEPC allows much aggressive vertex system design, a detailed vertex optimization study could be found in section **??**.

1.3 Detector concepts

1.3.1 The baseline detector concept

To address these physics requirements, a Particle Flow Oriented detector concept has been developed as the CEPC baseline detector, see Fig. 1.10. The Particle Flow principle, in short, interprets all the detector signal as the final state particles. For each physics event, all the physics objects are reconstructed from an unique list of final state particles. The single particle level physics objects, for example the leptons, the photons, and the kaons, are identified directly from the final state particle list. The composited physics objects, for example the converted photons, the K_s^0, the τ lepton and the jets, are identified using dedicated finding algorithm such as tau finder and jet clustering algorithms. Subtracting the total visible four-momentum of all the final state particle from the initial four momentum determines the missing four-momentum. This global interpretation of the final state particles leads to high efficiency, and high purity reconstruction of all the physics

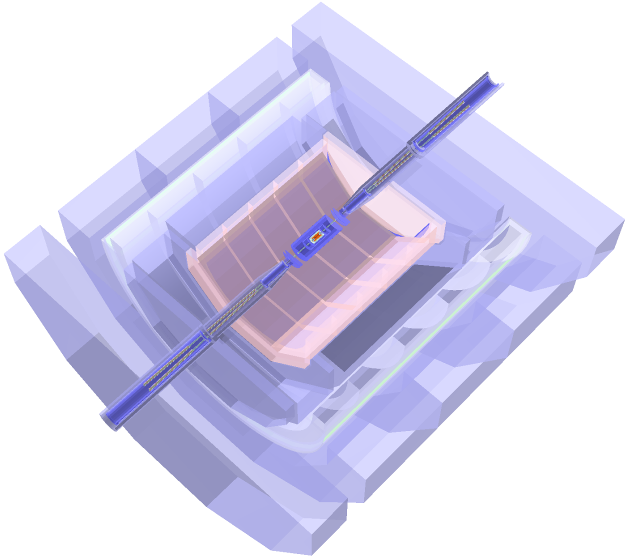

Figure 1.10: Sliced view of the APODIS detector concept, the baseline detector geometry for the CEPC CDR study. The APODIS uses double beam with 33 mrad cross angle, and have a short L* of 2.2 meter. In its Barrel, from inner to outer, the APODIS detector is composed of a Vertex system (Red), a Silicon Inner Tracker (Deep Blue), a TPC, a Silicon External Tracker, a ECAL (Pink), a HCAL (Violet), a Solenoid of 3 Tesla and a Return Yoke. In its forward region, 5 pairs of tracking disks is installed to enlarge the detector acceptance.

objects. In addition, the Particle Flow algorithm in principle associate the detector hits to each individual particle, therefore, the final state particle could be measured in the most-suited sub-detector system. For the charged particles, the relative accuracy of track momentum resolution at the tracking system is usually much better than the energy resolution at calorimeter system at the APODIS. Therefore, the Particle Flow algorithm also significantly improves the accuracies on the energy reconstruction of composed objects, especially for the τ lepton and the jets.

The baseline detector geometry is named APODIS, stands for A Particle Flow Oriented Detector for the HIggS factory. APODIS is optimized from the CEPC v_1 geometry, the reference detector geometry for the CEPC PreCDR studies. The CEPC v_1 is developed from the concept and International Large Detector (ILD), the baseline detector for the linear collider studies. Comparing to the CEPC v_1, the APODIS enhances the performance on the identification of charged Kaons; maintains the same performance on the Higgs measurements, meanwhile, it has significantly reduce the construction cost and the power consumption.

From inner to outer, the APODIS is composed of a silicon pixel vertex system, a silicon internal tracker, a TPC main tracker, a Silicon-tungsten sampling ECAL, a Iron-Glass Resistive Plate Chamber HCAL, a solenoid, and a return Yoke.

The APODIS has a dedicated design on the forward region and the MDI. The L* of APODIS has a length of 2.2 meters, and a compensation solenoid system is installed at z position of 1100 - 6000 mm. A LumiCal is installed at the end of this nose. A compact, forward tracking system composed of 5 pairs of tracking disks is installed in between z position of 200 - 1000 mm.

The solenoid B-Field of the APODIS is 3 Tesla. The CEPC uses double ring configuration, with a cross angle of 33 mrad at the interaction point. Each time the bunch passing through the detector, the beam emittance increases via the coupling to the detector solenoid B-Field (especially the vertical emittance). In order to achieve a high luminosity, this solenoid B-Field needs to be compensated locally. Therefore, a compensating solenoid is installed in the forward region of the CEPC detector. Considering the technology challenge of the compensating solenoid and the physics requirement at the CEPC, APODIS uses a solenoid of 3 Tesla for the CEPC Higgs operation, and the central solenoid might be further reduced to 2 Tesla for the CEPC Z pole operation.

The APODIS uses the Time Projection Chamber (TPC) as its main tracker. The TPC provides good energy resolution, excellent track reconstruction efficiency, low material budgets, and its dE/dx measurement is essential for the particle identification, see section **??**. On the other hand, compared to the silicon tracking, the TPC is a slow technology: the drift time of ions is of the order of one second at the APODIS TPC. At TPC, both primary ionization of charged tracks and ion backflow from the amplification procedure generates ions, which accumulate in the gas volume. These ions will distort the drift electric field and eventually limit the precision of track momentum measurement. The physics event rate at the CEPC Z pole operation is of the order of 10^{3-4} Hz, therefore, ions generated from thousands of events pile up in the gas volume. The control of backflow ion is then essential for the TPC operation.

Iterated with the hardware R&D, dedicated simulation studies are performed at the CEPC TPC study. Using double amplification layer, the ion backflow could be controlled to per mille level without gating [**?**]. On the other hand, the simulation analysis shows that at this level of ion backflow control, the degrading of spatial point resolution is smaller than the intrinsic TPC spatial resolution. The TPC occupancy is also analyzed at the TPC Z pole. Those studies lead to the conclusion that the TPC is a feasible technology option for the CEPC [**?**].

The TPC in the APODIS has an inner radius of 0.3 meters, an outer radius of 1.8 meters, and a length of 4.7 meters. It is divided into 220 radical layers, each has a thickness of 6 mm. Along the ϕ direction, each layer is segmented into 1 mm wide cells. In total, the TPC has 10 million readout channels in each endcap. Operating in 3 Tesla solenoid B-Field, the TPC provides a spatial resolution of 100 μm in the $R - \phi$ plane and 500 μm resolution in the Z direction for each tracker hit. The TPC reaches a standalone momentum resolution of $\delta(1/P_t) \sim 10^{-4}\mathrm{GeV}^{-1}$.

The APODIS is equipped with large-area silicon tracking devices, including the pixel vertex system, the forward tracking system, and the silicon inner/external tracking layers located at the boundary of the TPC. Combining the measurements from the silicon tracking system and the TPC, the track momentum resolution could be improved to $\delta(1/P_t) \sim 2 \times 10^{-5}\mathrm{GeV}^{-1}$. In fact, the TPC is mainly responsible for the pattern recognition and track finding, while the silicon tracking devices dominate the momentum measurement. The silicon pixel vertex system also provides precise impact parameter resolution ($\sim 5\mu\mathrm{m}$), which is highly appreciated for the τ lepton reconstruction and the jet flavor tagging.

The APODIS uses high granular sampling Electromagnetic Calorimeter (ECAL) and Hadronic Calorimeter (HCAL). The calorimeter is responsible for separating final state particle showers, measuring the neutral particle energy, and providing information for the lepton identification [**?**][**?**]. The entire ECAL and HCAL are installed inside the

Concept	ILD	CEPC v_1	APODIS
Solenoid B-Field/Tesla	3.5	3.5	3
L*/m	3.5	1.5	2.2
Pairs of forward tracking disks	7	5	5
ECAL Cell Size/mm	5	5	10
ECAL Time resolution/ns	-	-	200 ps/hit
HCAL Layer Number	48	48	40
HCAL Absorber thickness/m	1.3	1.3	1.0
Total Weight/kton	15	10	8

Table 1.2: Comparison of detector parameters

solenoid, providing 3-dimensional spatial position and the energy information. The ECAL geometry parameter is determined by a dedicated optimization study [**?**]. The ECAL is composed of 30 layers of alternating silicon sensor and tungsten absorber. It has a total absorber thickness of 84 mm. Transversely, each sensor layer is segmented into 10 mm by 10 mm cells. The HCAL uses Resistive Plate Chamber sensor and Iron absorber. It has 40 longitudinal layers, each consists of a 25 mm Iron absorber. Transversely, it is segmented into 10 mm by 10 mm cells.

This calorimeter system provides decent energy measurement for the neutral particles (i.e. roughly $16\%/\sqrt{E/\mathrm{GeV}}$ for the photons and $60\%/\sqrt{E/\mathrm{GeV}}$ for the neutral hadrons). More importantly, it records enormous information of the shower spatial development, ensuring efficient separation between nearby showers and providing essential information for the lepton identification, see section **??**. In addition, the silicon tungsten ECAL could provide precise time measurement. Requesting a cluster level time resolution of 50 ps, the ECAL Time of Flight (ToF) measurement plays a complementary role to the TPC dE/dx measurement, leading to a decent charged Kaon identification performance, see section **??**.

Table 1.2 listed the main parameters of ILD, CEPC v_1 and the APODIS. As will be introduced in the following chapter, the APODIS maintains the same performance for the CEPC Higgs measurements comparing to CEPC v_1. Meanwhile, the total cost, the total weight, and the calorimeter thickness have been significantly optimized (by 25%, 30% and 20% respectively). In addition, APODIS has a good performance in charged kaon identification, which is highly appreciated in the flavor physics and in the jet flavor/charge reconstruction.

1.3.2 Full silicon detector concept

1.3.3 An alternative low magnetic field detector concept

The baseline detector described in this CDR is a very straightforward evolution of the ILD detector originally conceived for the International Linear Collider (ILC) [1]. We propose here a new detector concept, IDEA, that is specifically designed for CepC and also attempts to significantly reduce the overall cost of the detector.

While most detector requirements needed for detectors at ILC are very similar to those for CepC [2], there are however some notable differences. First of all the typical luminosity expected both at the Z pole ($\sqrt{s} = 90\,GeV$) and above the ZH threshold ($\sqrt{s} = 240\,GeV$) is expected to be one or two orders of magnitude larger, with a much shorter bunch spacing and no large time gaps in the beam structure. This places severe constraints on the tracking system. In particular one would prefer an intrinsically fast main tracker to fully exploit the cleanliness of the e^+e^- environment, and a very low power vertex detector, since power pulsing is not allowed by the bunch spacing. Additional issues of emittance preservation, typical of circular machines, set limits on the maximum magnetic field usable for the tracker solenoid, especially when running at the lower energy. This could be a problem for a large volume TPC, due to the resolution degradation, and also for a silicon tracker, since it would require more layers at a large radius, thus significantly increasing the cost.

Additional specific requirements on a detector for CepC come from precision physics at the Z pole, where the statistical accuracy on various electro-weak parameters is expected to be an order of magnitude better than at the ILC. This calls for a very tight control of the systematic error on the acceptance, with a definition of the acceptance boundaries at the level of a few μm, and a very good $e\!-\!\gamma\!-\!\pi_0$ discrimination to identify τ leptons efficiently and measure their polarization. A pre-shower, with the first measurement layer based on silicon micro-strip detectors, just outside the tracker, could be an effective solution, while at the same time improving the overall tracking system resolution.

The particle flow calorimeters currently proposed for both ILC and CLIC, are very expensive due to their extremely large number of readout channels and require significant data processing to obtain the optimal performance. A cheaper and more effective calorimeter can be made using the dual readout technique [3], which has been extensively studied and demonstrated in over ten years of R&D by the DREAM/RD52 collaboration [4, 5]. With this technology the electromagnetic and hadronic calorimeters come in a single package that plays both functions and allows an excellent discrimination between hadronic and electromagnetic showers [6].

Finally recent developments in multi-pattern gas detector technology, such as μRwell [7], can significantly reduce the cost of large area tracking chambers to be used for tracking muons outside the calorimeter volume.

1.3.3.1 The IDEA detector

The structure of the IDEA detector is outlined in figure 1.11.

A key element of IDEA is a thin, ∼30 cm, and low mass, $\sim 0.8\,X_0$, solenoid with a magnetic field of 2 Tesla. This field is optimal, according to studies done for FCC-ee, as it minimizes the impact on emittance growth and allows for manageable fields in the compensating solenoids [8], but is certainly too low to support a TPC or a silicon tracker of reasonable size.

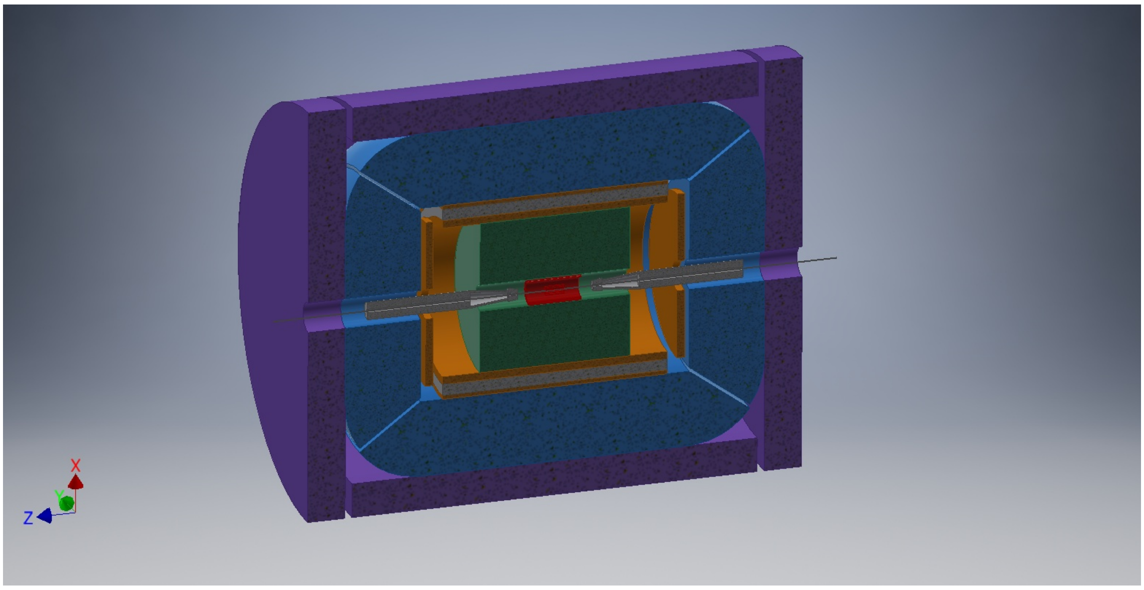

Figure 1.11: Schematic layout of the IDEA detector. Sub-detectors are outlined in different colors : vertex detector (red), drift chamber (green), pre-shower (orange), magnet (gray), calorimeter (blue), magnet yoke and muon system (violet).

The innermost detector, surrounding the 1.5 cm beam pipe, is a silicon pixel detector for the precise determination of the impact parameter of charged particle tracks. Recent test beam results on the detectors planned for the ALICE inner tracker upgrade (ITS), based on the ALPIDE readout chip [9], indicate an excellent resolution, $\sim$5 μm, and high efficiency at low power and dark noise rate [10]. This looks like a good starting point for the IDEA vertex detector and is a similar approach is proposed for the CepC baseline detector (see section 4.5). The two detector concepts could then share the same pixel technology as well as profit from the electronic and mechanical work of the ALICE ITS.

Outside the vertex detector we find a 4 m long cylindrical drift chamber starting from a radius of $\sim$30 cm and extending until 2 m. The chamber can be made extremely light, with low mass wires and operation on 90% helium gas; less than 1% X_0 is considered feasible for 90° tracks. Additional features of this chamber, which is described in detail in section 6.3, are a good spatial resolution, $<$100 μm, dE/dx resolution at the 2% level and a maximum drift time of only 150 nsec. Track momentum resolution of about 0.5% for 100 GeV tracks is expected when vertex detector and pre-shower information is included in the track fit. It is worth noting that the design of this chamber is the evolution of work done over many years on two existing chambers, that of the KLOE detector [11] and that of the recent MEG experiment upgrade [12]; major R&D work was done also for the 4th concept at ILC [13] and then for the Mu2E tracker [14].

A pre-shower is located between the drift chamber and the magnet in the barrel region and between the drift chamber and the end-cap calorimeter in the forward region. This detector consists of a $\sim$1 X_0 = 0.5 cm of lead followed by a layer of silicon micro-strip detectors. A second layer of MPGD chambers is located between the magnet and the calorimeter in the barrel region, while in the end-cap region an additional layer of lead is placed between the silicon and the chambers. This way about 75% of the π^0's can be tagged by having both γ's from their decay identified by the pre-shower. The silicon layer, besides increasing the tracking resolution, provides a very precise acceptance determination for both charged particles and γ's. The optimization of pre-shower thickness and calorimeter resolution is still in progress.

A solenoidal magnet surrounds the tracking system and the first pre-shower layer. Presently planned dimensions are 6 m of length and 4.2 m inner diameter. The relatively low two Tesla field and the small dimensions have important implications on the overall magnet package thickness, that can be kept at the 30-40 cm level, and on the size of the flux return yoke, which scales linearly with the field and the square of the coil diameter. With the given dimensions a yoke thickness of less than 100 cm of iron is sufficient to completely contain the magnetic flux and provide adequate shielding and support for the muon chambers.

A dual readout fiber calorimeter (see section 7) is located behind the second pre-shower layer. We assume a total calorimeter depth of 2 m, corresponding to approximately eight pion interaction lengths. The detector resolution is expected to be about $10.5\%/\sqrt{E}$ for electrons and $35\%/\sqrt{E}$ for isolated pions with negligible constant terms, as obtained from extrapolations from test beam data using GEANT4 without including the pre-shower. This detector has very good intrinsic discrimination between muons, electrons/photons and hadrons for isolated particles [6]. This discrimination power is further enhanced when the information of the pre-shower and the muon chambers is added, extending the separation power also into hadronic jets and making it suitable for the application of particle-flow-like algorithms. The intrinsic high transverse granularity provides a good matching of showers to tracks and pre-shower signals.

The muon system consists of layers of muon chambers embedded in the magnet yoke. The area to be covered is substantial, several hundreds of square meters, requiring an inexpensive chamber technology. Recent developments in the industrialization of μRwell based large area chambers, as planned for the CMS Phase II upgrade, are very promising (see section 9).

1.3.3.2 Conclusions

A different concept for a detector at CepC has been proposed. This detector is designed specifically for CepC and its specific running conditions and physics goals. In particular it is safe with respect to interaction between the detector solenoid field and the beam. Although additional R&D to optimize performance, reduce costs and come to a detailed engineered design of the detector is still necessary, this detector is based on technologies which are established after many years of R&D and whose feasibility has by large been established. Furthermore several choices are made to simplify the detector structure and reduce the cost, which in the end should be significantly smaller than for an ILD-like detector.

References

[1] H. Abramowicz et al., *The International Linear Collider Technical Design Report - Volume 4: Detectors*, arXiv:1306.6329 [physics.ins-det].

[2] C.-S. S. Group, *CEPC-SPPC Preliminary Conceptual Design Report. 1. Physics and Detector*, .

[3] DREAM Collaboration, R. Wigmans, *The DREAM project: Towards the ultimate in calorimetry*, Nucl. Instrum. Meth. **A617** (2010) 129–133.

[4] N. Akchurin et al., *The electromagnetic performance of the RD52 fiber calorimeter*, Nucl. Instrum. Meth. **A735** (2014) 130–144.

[5] RD52 (DREAM) Collaboration, R. Wigmans, *New results from the RD52 project*, Nucl. Instrum. Meth. **A824** (2016) 721–725.

[6] N. Akchurin et al., *Particle identification in the longitudinally unsegmented RD52 calorimeter*, Nucl. Instrum. Meth. **A735** (2014) 120–129.

[7] M. Poli Lener, G. Bencivenni, R. de Olivera, G. Felici, S. Franchino, M. Gatta, M. Maggi, G. Morello, and A. Sharma, *The μ-RWELL: A compact, spark protected, single amplification-stage MPGD*, Nucl. Instrum. Meth. **A824** (2016) 565–568.

[8] M. Koratzinos et al., *Progress in the FCC-ee Interaction Region Magnet Design*, http://inspirehep.net/record/126211/files/wepik034.pdf (2017) , IPAC2017.

[9] ALICE Collaboration, M. Mager, *ALPIDE, the Monolithic Active Pixel Sensor for the ALICE ITS upgrade*, Nucl. Instrum. Meth. **A824** (2016) 434–438.

[10] ALICE Collaboration, G. Aglieri Rinella, *The ALPIDE pixel sensor chip for the upgrade of the ALICE Inner Tracking System*, Nucl. Instrum. Meth. **A845** (2017) 583–587.

[11] KLOE Collaboration, A. Calcaterra, *The KLOE drift chamber*, Nucl. Instrum. Meth. **A367** (1995) 104–107.

[12] MEG Collaboration, Y. Uchiyama, *Upgrade of MEG experiment*, PoS **EPS-HEP2013** (2013) 380.

[13] A. Mazzacane, *The 4th concept detector for the ILC*, Nucl. Instrum. Meth. **A617** (2010) 173–176.

[14] L. De Lorenzis, F. Grancagnolo, A. L'Erario, A. Maffezzoli, A. Miccoli, S. Rella, M. Spedicato, and G. Zavarise, *Analysis and Characterization of the Mechanical Structure for the I-Tracker of the Mu2e Experiment*, Nucl. Phys. Proc. Suppl. **248-250** (2014) 134–136.

./

CHAPTER 2

PHYSICS PERFORMANCE

2.1 Introduction

The physics performance is determined by the detector geometry and the reconstruction algorithms. A Particle Flow Algorithm Arbor is optimized for the APODIS and a full simulation-reconstruction software chain(cepcsoft) has been developed. Using APODIS detector geometry and the cepcsoft, the physics performance is evaluated at the full simulation level. The cepcsoft and Arbor in briefly introduced in section 2.2, In section 2.3, the physics performance is summarized at physics object level, and with corresponding Higgs signal distributions.

2.2 The CEPC Software and the Arbor

The reconstruction is vital for the high energy physics experiment. Comparing to the conventional reconstruction at the collider experiments, the Particle Flow reconstruction interprets the information from every subsystem coherently and is much complicated. A Particle Flow algorithm, Arbor [**?**], has been developed, and an entire simulation-reconstruction software chain (cepcsoft [**?**]) has been established accordingly.

The cepcsoft developments starts from the ilcsoft [**?**], the software framework & toolkit for the linear collider studies. It uses the same data structure and management (LCIO and Marlin [**?**]), the tracking and flavor tagging modules from the ilcsoft. It also uses several general high energy physics softwares such as the Geant4, the Whizard [**?**], the Madgraph [**?**], the Pythia [**?**], and the Delphes [**?**]. Many dedicated software tools are developed and integrated into the cepcsoft. The information flow and essential modules are introduced in section 2.2.1. The Arbor algorithm is presented in section 2.2.2.

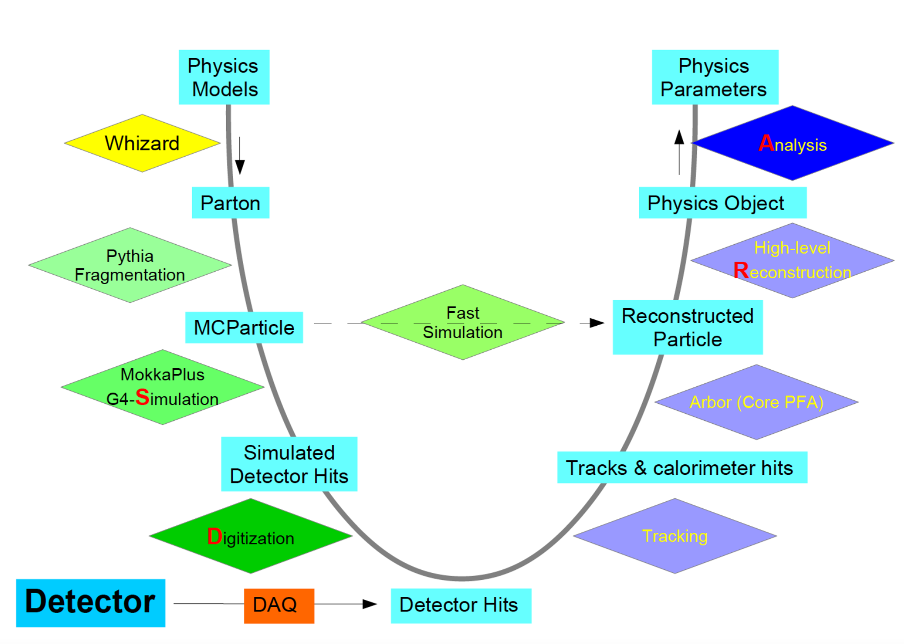

Figure 2.1: Information flow at CEPC simulation studies

2.2.1 The cepcsoft

The information flow at the CEPC simulation-reconstruction is shown in Fig. 2.1. The starting point is the generator softwares. In the full simulation, the generator samples are processed to Geant4 simulation, which generates simulated detector hits that record the energy deposition information in sensitive volumes of the virtual detector. These simulated detector hits are digitized into detector hits, by convoluting the sub-detector responses to the energy deposition information. In the ideal case, the digitized hits should be indistinguishable from the experimental data, and the following reconstruction modules treat them indifferently.

The reconstruction modules include the tracking, the Particle Flow, and the high level reconstruction algorithms. The digitized tracker hits are reconstructed into tracks via the tracking modules. The particle flow algorithm reads the reconstructed tracks and the calorimeter hits, and builds reconstructed particles. The single particle level physics objects, like the leptons, the photons, and the kaons, are identified directly. Subtracting the initial 4-momentum of the system with the accumulated four-momentum of every final state particle leads to the reconstruction of the missing energy and momentum. High level reconstruction algorithms are applied to reconstruct compound physics objects such as the converted photons, the K_ss, the τ leptons, and the jets. Once the jets are identified, the jet flavor tagging algorithm, jet charge measurement algorithm are applied accordingly. The physics observables could then be constructed via the algebraic combinations of the kinematic variables of these physics objects.

From the technical point of view, the cepcsoft is composed of fourteen independent modules:

1, The generator: the Whizard [?], the Madgraph [?], and the Pythia [?]. The Whizard is a widely used generator for the linear collider studies. In cooperating with the whizard team, dedicated CEPC beam parametrization has been established in its official release. The Whizard generator is used for the SM processes, including both Higgs signal and all the SM backgrounds [?]. Meanwhile, Madgraph and Pythia are used to generate New Physics samples.

2, The data format and the data management. CEPC software uses the data format (LCIO) and data management (Marlin) inherited from the ilcsoft.

3, The simulation: the MokkaPlus [?]. MokkaPlus is a virtual geometry constructor that compiled with the Geant4 libraries [?] and mysql database [?]. The MokkaPlus is developed from the Mokka [?], the obsoleted simulation framework used in linear collider studies (The linear collider simulation has moved to the recent development of DD4HEP [?], however, depends on the software robustness and on the available manpower, we decided to continue developing MokkaPlus). Many new functions have been added to the MokkaPlus and all the CEPC detector models are implemented into MokkaPlus.

4, The digitization algorithms. The digitization algorithm should properly model the amplification procedure and the time-dependent patterns of the sub-detector. These dedicated models need to be established and tuned according to experimental data. The digitization algorithm is sub-detector dependent and technology dependent. We developed a general calorimeter digitization algorithm for both APODIS ECAL and HCAL, which could precisely reproduce the test beam results [?]. The tracker digitization modules are inherited from the ilcsoft, whose parameters are adjusted for the optimization studies to the sub-detectors.

5, The tracking algorithm. The CEPC software uses the entire tracking module from the ilcsoft, which is proved to be very efficient. In addition, a dedicated CEPC tracking algorithm is under developing, the preliminary results look promising [?].

6, The particle flow algorithm. The particle flow algorithm is the core of the CEPC reconstruction. We developed Arbor algorithm and optimize it for the APODIS detector. More detailed information and typical performance will be given in following sections.

7, The single particle level physics object finding algorithms. Dedicated lepton identification (LICH [?]) and photon identification algorithms have been developed. These algorithms have been integrated into Arbor. The performance will be presented in section 2.3.

8, The composed object finder. Coral, a simple algorithm that targets at a general simple composed object finder, is in the early developing and testing phase. Coral target at a high efficiency reconstruction of converted photon, π_0, K_s, *etc*.

9, The tau finding algorithm. A dedicated tau finder has been developed, see [?]. Details will be giving in section 2.3.

10, The jet clustering algorithm. Fastjet [?] package has been used in CEPC software.

11, The jet flavor tagging algorithm. CEPC software uses the official flavor tagging algorithm, LCFIPlus [?], from the ilcsoft.

12, The Event Display. We developed Druid [?], one of the official linear collider event display software. Druid has been adjusted to the CEPC studies by including dedicated display setup and geometry files. All the displays demonstrated in this paper is produced by Druid.

13, The general analysis framework. FSClasser [?], a general physics analysis framework that automatically calculates the kinematic observables for most of the physics objects, is developed and integrated into CEPC software.

14, The fast simulation. Two fast simulation packages have been developed and validated with the full simulation. The first one is developed using LCIO-Marlin framework, used mainly for the massive processing of SM background for the physics analysis. The second is developed based on the Delphes software, and integrated into its official releases [?] [?].

To conclude, a fully functional simulation-reconstruction software chain, the cepcsoft has been established for the CEPC detector design studies. The cepcsoft is developed from the ilcsoft [?] and integrates many novel developments. Among all fourteen independent modules of the cepcsoft, we developed eight modules (including Arbor) and adjusted two modules (the MokkaPlus and the Digitization) for the CEPC study. Three essential modules, the LCIO-Marlin framework, the tracking and the flavor tagging, are inherited from the ilcsoft. Meanwhile, some of our efforts are also integrated to ilcsoft, such as the LICH [?], the Digitization [?], and the event display [?]. The CEPC software uses other open source softwares such as the generator and the fast simulation, to which we have established collaboration with the developer.

2.2.2 Arbor

The Particle Flow algorithm, Arbor [?][?], has been optimized for the APODIS detector concept.

Inspired by the simple fact that the tree configuration of particle shower, Arbor creates oriented connectors between calorimeter hits, and iterates (creating/removing connectors and swap their directions) until the connector-hit ensemble follows a tree topology. The branches hence represent the trajectories of charged shower particles. The seeds usually correspond to the impact position of the particle at the calorimeter. Since the separation of the seeds is straightforward, Arbor efficiently separates the particle showers, which is highly appreciated by the Particle Flow principle.

Arbor is composed of a calorimeter clustering module and a matching module. The clustering module reads the calorimeter hits and builds the calorimeter clusters. The matching module identifies the calorimeter clusters induced by charged particles (charged clusters), combines these clusters with tracks, and builds charged reconstructed particles. The remaining clusters are reconstructed into photons, neutral hadrons, and fragments (mainly from charged clusters). The final state particles are therefore reconstructed.

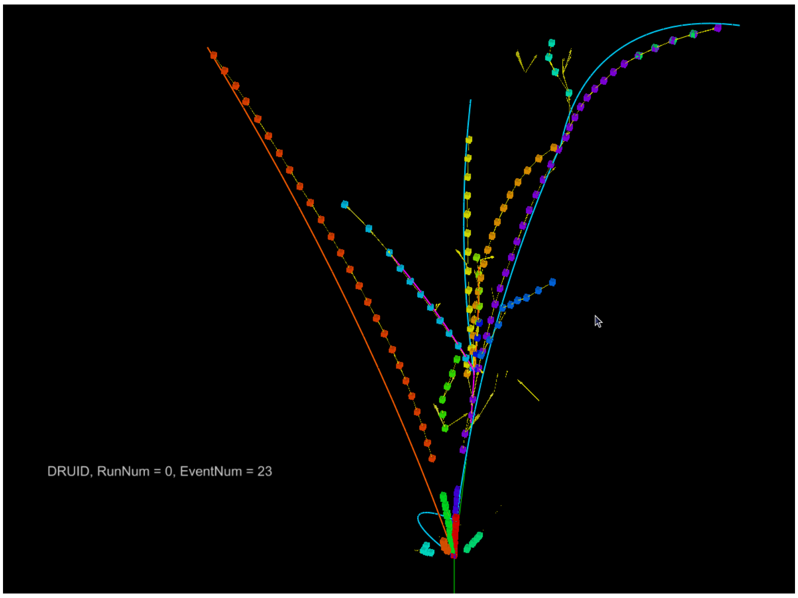

Figure 2.2: K_L shower reconstructed by the Arbor algorithm, the branches – the calorimeter hit clusters – are corresponding to the trajectories of charged particles generated in the shower cascade.

Fig. 2.2 shows a reconstructed calorimeter shower of a 20 GeV K_L^0 particle at the high granularity calorimeter, where the readout density is roughly 1 channel/cm^3. The reconstructed tree branches are demonstrated with different colors. Therefore the trajectory length of charged shower particle can be reconstructed. Fig. 2.3 compares the reconstructed trajectory length with MC truth, the red distribution is the MC truth level trajectory length of charged particles generated inside 40 GeV π showers; the green one is corresponding to the trajectory of the electron and the positron generated in the showers; while the blue is the trajectory length reconstructed by Arbor. Good agreement between the reconstruction and MC truth is found at sufficient trajectory length.

Arbor can also be characterized by the energy collection performance at single neutral particle and the separation performance at bi-particle samples. Typically, Arbor reaches an energy collection efficiency higher than 99% for photons with energy higher than 5 GeV at the APODIS geometry. Higher hit collection efficiency usually leads to a better energy resolution but also increases the chance of confusions, i.e, the wrong clustering of calorimeter hits.

Excellent separation performance is crucial for the jet energy reconstruction, the π^0 reconstruction, and the measurement with τ final states. This performance can be characterized via the reconstruction efficiency of di-photon samples, where two photons with the same energy are shot in parallel at different positions, see Fig. 2.4. According to the distribution of π^0 energy at $Z \rightarrow \tau^+\tau^-$ events at CEPC Z pole operation, we set the photon energy to 5 GeV.

The reconstruction efficiency is defined as the probability of successfully reconstructed two photons with anticipated energy (each candidate is required to have an energy within 1/3 to 2/3 of the total induced energy). The efficiency curve naturally exhibits an S-curve dependency on the distance between the photon impact positions, see Fig. 2.5. The distance at which 50% of the events are successfully reconstructed is referred to as the

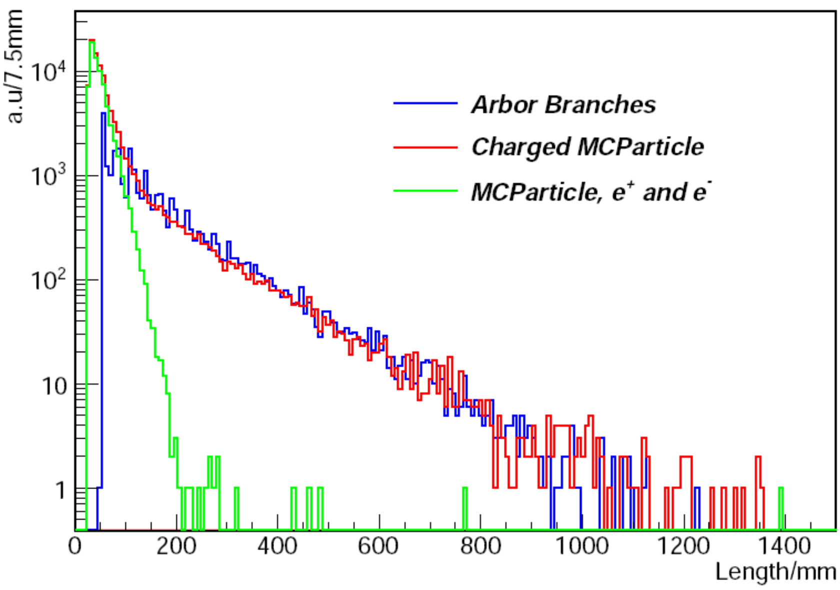

Figure 2.3: Proof of Principle: reconstructed and MC truth particle trajectory length at 40 GeV π showers.

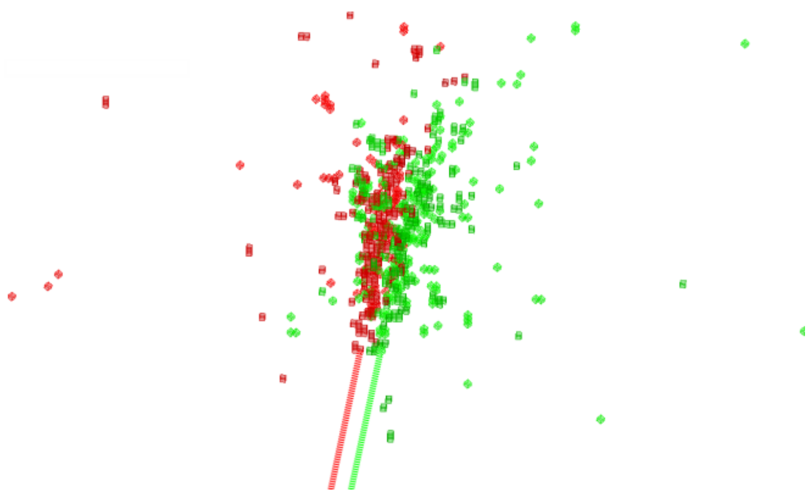

Figure 2.4: A reconstructed di-photon event at Si-W ECAL with 1 mm cell size. Each photon has an energy of 5 GeV, and their impact points are separated by 4 mm.

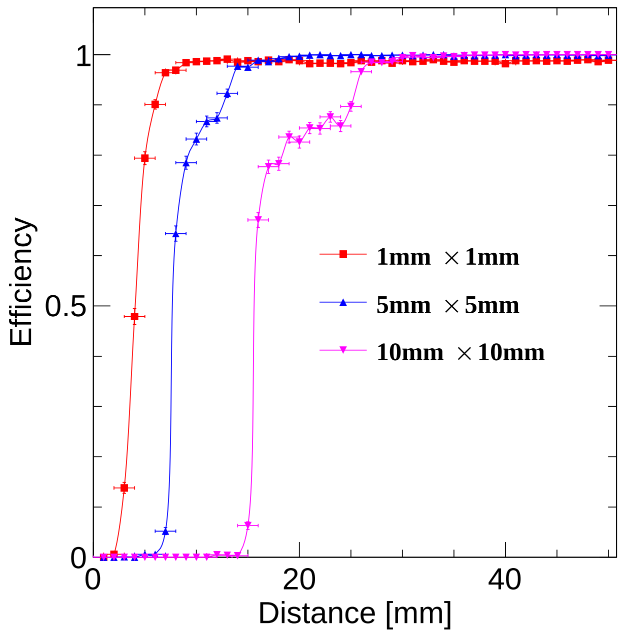

Figure 2.5: Reconstruction efficiency of the di-photon events at different ECAL cell sizes. The X-axis represents the distance between photon impact points.

ECAL cell size	Critical distance for separation
1 mm	4 mm
5 mm	9 mm
10 mm	16 mm

Table 2.1: Arbor critical separation distance at di-photon sample with different ECAL cell size.

critical distance, which depends on the ECAL transverse cell size. At the cell size smaller than the Moliere radius, the critical distance is roughly 2 times the cell size, see Table. 2.1.

To conclude, Arbor is a geometrical algorithm that reconstructs each shower cluster into a tree topology. At high granularity calorimeter, Arbor efficiently separates nearby particle showers and reconstructs the shower inner structure. It maintains a high efficiency in collecting the shower hits/energy, which is appreciated by the neutral particle energy reconstruction.

To conclude, Arbor, a Particle Flow algorithm that responsible for reconstructing all the final state particles, has been developed for the CEPC studies. A full reconstruction chain has been developed based on Arbor. Arbor could efficiently separate nearby particle showers and reconstructs the shower inner structure. The separation performance is efficiently good that almost all the final state particles could be safely treated as well separated for the CEPC Higgs measurements, which is essential for the Particle Flow reconstruction, and also enables a reliable and straightforward modeling of fast simulation.

The physics performances will be discussed in the following sections. All the samples, unless explicitly stated, are simulated at APODIS and reconstructed with the cepcsoft.

2.3 Performance at the Physics Object level

This section gives a global description of the reconstruction of core physics objects at the CEPC: the leptons, the photons, the kaons, and the jets. The reconstruction of the τ leptons is addressed in the next section **??**, where a full simulation analysis on the $\sigma(XH) * Br(H \rightarrow \tau^+\tau^-)$ is presented. Before we goes into these physics object, a comprehensive diagnosis on the tracking performance is reported.

2.3.1 Tracking performance

The APODIS tracking system is composed of a TPC main tracker and a silicon tracking system. These two subsystems play complementary roles. The TPC has more than 200 radial layers, and has a high efficiency track finding performance. The silicon devices provide high precision spatial point measurements. Comparing to a standalone TPC, this combination improves significantly the tracking momentum resolution, especially for high energy tracks. In addition, the silicon tracking system includes a forward tracker that increases significantly the solid angle coverage of the tracker.

This section presents the tracking performance on two samples: a single muon particle gun sample and a $Z \rightarrow \tau^+\tau^-$ sample corresponding to the CEPC Z pole operation. The particle gun sample describes the tracking efficiency and accuracies for isolated tracks. And the $Z \rightarrow \tau^+\tau^-$, with one of the τ lepton decays into 3 prong final states, provides a critical test for the separation performance of nearby tracks. These samples are reconstructed with Clupatra, the tracking module at the ilcsoft [**?**].

The single muon particle gun sample has a total statistic of 10 million, and covers a momentum range from 0.1 GeV to 100 GeV. Fig. 2.6 shows the extracted differential efficiency and resolution on the polar angle and the particle energy. Clearly, once the energy is larger than 0.5 GeV, and the track is within tracker fiducial region of $|cos(\theta)| < 0.985$, the tracking efficiency converges 100%. While the relative accuracy of transverse momentum resolution reaches per mille level for the energy range of 10 - 100 GeV.

The CEPC Z pole operation provides very clean $Z \rightarrow \tau^+\tau^-$ signal. About 10% of the τ lepton decays into 3-prong final states. A typical event is displayed in Fig. 2.7. Since the τ is highly boosted at the $Z \rightarrow \tau^+\tau^-$ events, the three charged particles decayed from the same τ lepton can be confined in a very narrow cone. Thus, these physics events pose stringent requirement on the nearby track reconstruction performance.

A dedicated $Z \rightarrow \tau^+\tau^-$ sample, with one τ decays into $2\nu\mu$ and the other into three charged pions and one neutrino. Defining the successful reconstruction efficiency as the probability of reconstructing three target tracks in these events with three visible pions in the events. The reconstruction efficiency is close to 100%.

To cross check the performance, two dedicated CEPC tracking algorithms are developed. The comparison shows consistent results is consistent with ilc tracking. A dedicated comparison report could be found in ref. [**?**][**?**].

To conclude, the tracking system at the APODIS provides a high efficiency, and high accuracy reconstruction of the track. In the tracker fiducial angle ($|cos(\theta)| < 0.985$), the reconstruction efficiency reaches 100% for tracks with momentum larger than 0.5 GeV. An overall reconstruction efficiency close to 100% has been achieved for $\tau \rightarrow 3\pi\nu$ sample. A dedicated analysis shows the charge misidentification rate is smaller than 10^{-4}, mostly

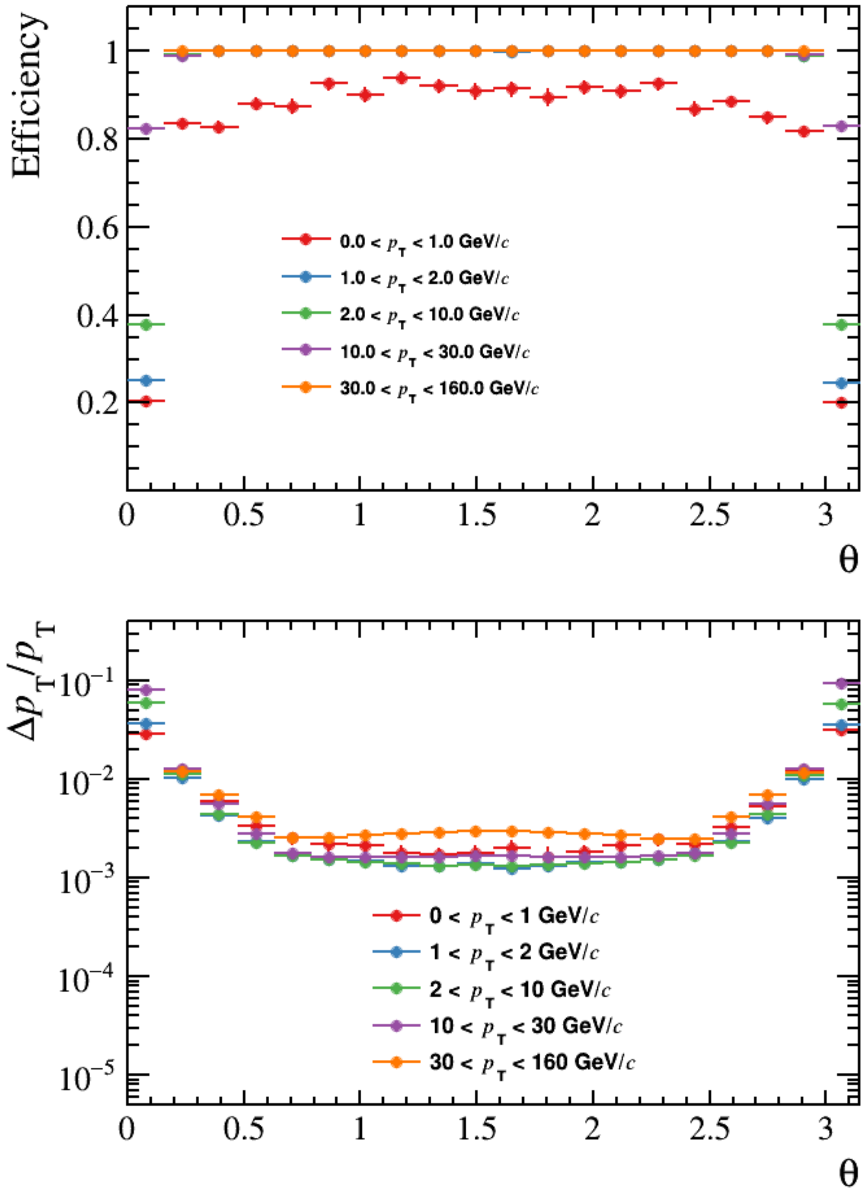

Figure 2.6: Single particle reconstruction efficiency (up plot) and resolution (lower plot) as a function of the track momentum and track polar angle.

concentrated at very forward region [?]. This tracking performance provides a solid starting point for the Particle Flow reconstruction at the APODIS.

2.3.2 Leptons

The lepton identification is of key importance to the CEPC Higgs program. First of all, about 7% Higgs boson events at the CEPC are generated together with a pair of leptons. Those events are the golden signals for the Higgs recoil analysis, which is the anchor for the absolute Higgs measurements. A significant fraction of the Higgs boson decays, directly or via cascade, into final states with leptons. 0.02% of SM Higgs decays into muons; the leptons serve as the essentially candles of identification of $H \to WW/ZZ \to$

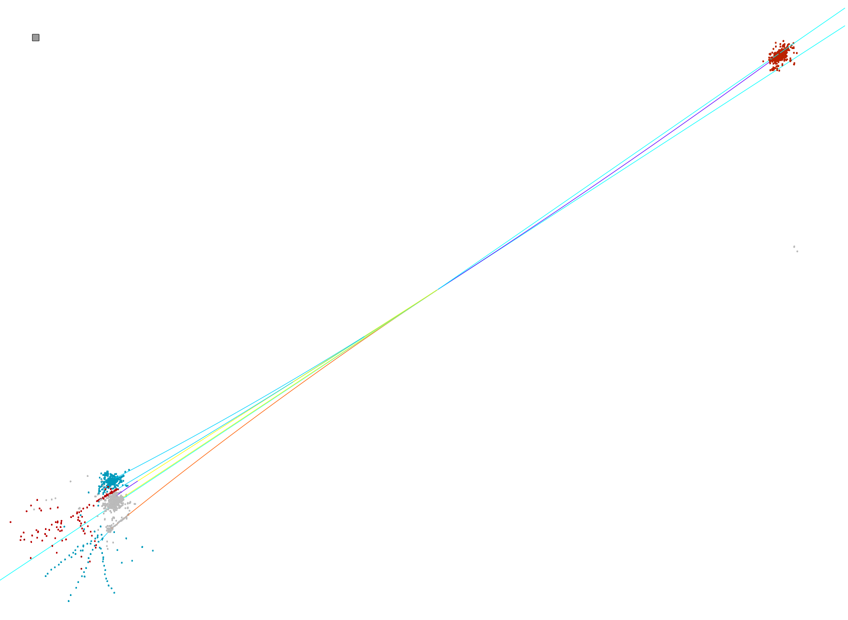

Figure 2.7: A simulated $Z \rightarrow \tau^+\tau^-$ event at CEPC Z pole operation. The left hand side τ lepton decays into 3 charged tracks, and 1 FSR photon. Through leptonic decay, the right handed one decays into an electron and two neutrinos.

leptonic/semi-leptonic final states. In addition, a significant fraction of Higgs->bb/cc events generate leptons in their decay cascade.

The PFA oriented detector, especially its calorimeter system, could provide enormous information for the lepton identification. In the CEPC v_4 geometry, a high-energy electron/positron/hadrons is likely to induce thousands of hits in the calorimeter with typical spatial configurations. Using the benchmark calorimeter geometry, the shower fractal dimension could be extracted [1]. In addition, the dE/dx measured by the TPC could efficiently separate electron/positrons from muon and hadrons, at track energy less than 10 GeV.

A dedicated Lepton identification algorithm for the detectors using high granularity calorimeter, LICH [2], has been developed. LICH extract more than 20 distinguish variables from the detector and combine these information into lepton-likelihood via MVA method. The performance of LICH have been scanned over a large range of the granularity for both ECAL and HCAL, while the performance is stable for particles with energy larger than 2 GeV.

At APODIS geometry, applied on isolated charged particle candidate with energy larger than 2 GeV, lepton identification efficiency better than 99.5% could be achieved with a mis-identification rate from hadrons is controlled to be smaller than 1%. This mis-identification is mainly induced by the irreducible background rate from pion decay (to muons) and highly electro-magnetic like pion clusters (via the pion0 generated from the pion-nuclear interactions). Not surprisingly, this performance is significantly better than that at LHC and LEP [**?**][**?**].

In the actual physics event, the lepton identification performance will be limited by the separation power of the detector. Using fully reconstructed llH events, we found the

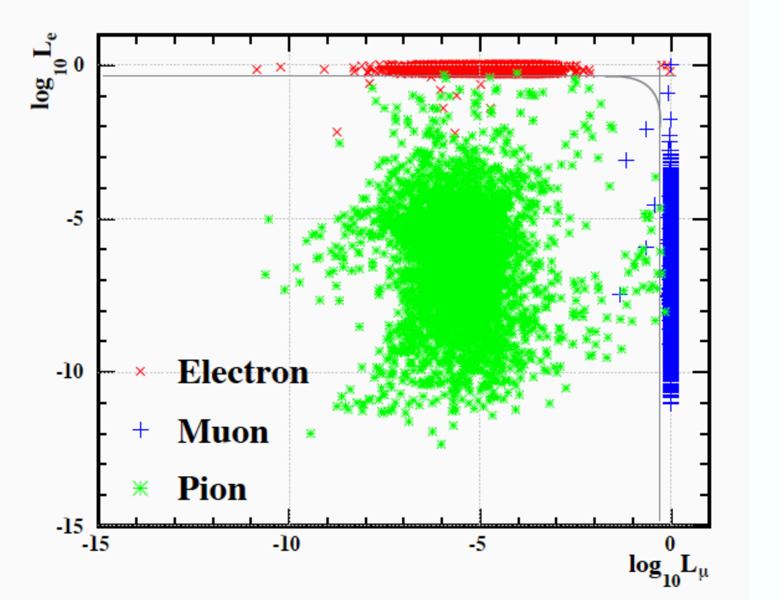

Figure 2.8: The distribution of charged particles in the phase space of calculated lepton likelihoods.

efficiency of successfully identify two leptons with opposite charge reaches 97-98%, In other word, less than 1% of the objective leptons in the llH events will potentially be mis-identified due to the overlapping of their cluster to the nearby showers. This result is consistent with the separation power of APODIS.

In terms of the Higgs signal at the CEPC, the tracking and the lepton identification performance can be characterized by the recoil mass distribution of l^+l^-H events and the invariant mass distribution of the $H \to \mu^+\mu^-$ events. These distributions are presented below.

2.3.2.1 Higgs recoil mass distribution at $\mu^+\mu^-H$ events

The Higgs recoil mass distributions at the l^+l^-H events are the most characteristic distributions of the electron positron Higgs factories. Since the initial 4-momentum is precisely known at the electron positron collider, and the pair of leptons (mostly generated from Z decay but also a few from the Z fusion events) could be precisely reconstructed, the recoil mass of Higgs boson could be calculated. Therefore, without any direct measurement on the Higgs boson decay final states, the Higgs signal could be identified by the characteristic recoil mass peak, whose position indicates the mass of Higgs boson and the total number of signal events is proportional to g^2_{HZZ}.

This distribution leads to a precise determination of the both Higgs boson mass and g_{HZZ}. The measurement of the Higgs boson mass is of strong physics interest itself. More importantly, the measurement of g_{HZZ} is unique at the electron positron Higgs factory. It anchors all the absolute Higgs boson measurements at the electron positron collider, and is highly complementary to the Higgs measurements operated at LHC and HL-LHC.

The di-muon recoil mass distribution is shown in Fig. 2.9. This distribution has a long high mass tail, induced by many radiation effects (the beamstrahlung, the bremsstrahlung, the final state radiation, and most importantly, the initial state radiation). The width of the peak distribution is determined by the intrinsic track momentum resolution and the beam energy uncertainty, both of which are at per mille level at the CEPC.

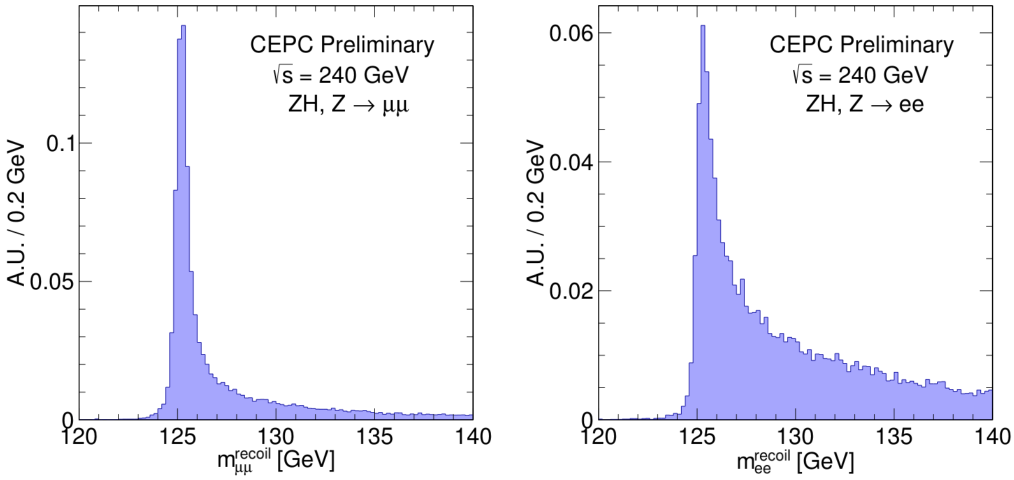

Figure 2.9: Recoil mass distribution of the $\mu^+\mu^-H$ and e^+e^-H events. Normalized to unit area.

In terms of the detector response, the recoil mass measurements require a high efficiency, high precision tracking system, good lepton identification performance.

2.3.2.2 The di lepton invariant mass distribution of $vvH, H \rightarrow \mu^+\mu^-$ events

CEPC could generate roughly 200 $H \rightarrow \mu^+\mu^-$ events. Thanks to the high precision tracking performance, the signal strength could be measured to a relative accuracy of 15% at the CEPC. The reconstructed di muon invariant mass distribution is shown in Fig. 2.10.

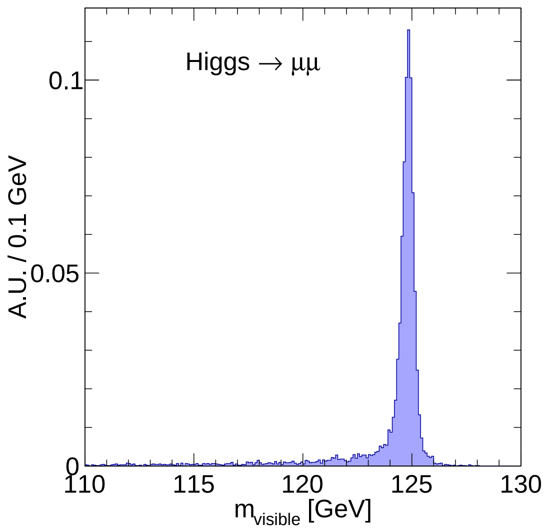

Figure 2.10: The reconstructed Higgs invariant mass of $H \rightarrow \mu^+\mu^-$ events at the CEPC v_1 detector geometry. 8k events, normalized to unit area.

Fig. 2.10 exhibits a low mass tail, induced mainly by the bremsstrahlung and FSR effects of the charged muon. In addition, the Higgs mass peak has a bias of 100 MeV, mainly induced from a tiny bias in the dEdx estimation in current simulation module.

2.3.3 Kaon Identification

Successful identification of the charged kaons is crucial for the flavor physics, and is highly appreciated in the determination of jet flavor and jet charge. According to the Bethe-Bloch equation, in the realistic energy range and at the same track momenta, the dEdx of pions is larger than that of kaons by roughly 10%. In other word, if the dEdx resolution could be measured to a relative accuracy better than 5%, the dEdx could leads to an efficient π-K separation.

The APODIS is equipped with a large TPC main tracker. Depending on the readout hardware performance, the dE/dx resolution leads to 2-4 σ π-K separation for 2-20 GeV charged tracks. See the left plot of Fig. 2.11. The upper boundary is the ideal separation predicted by the Geant4 simulation; while the lower boundary includes a 50% degrading with respect to the MCTruth, and is regarded as the conservative scenario. (A survey of the performance at previous experiments shows the degrading varies from 15% to 50%). The dE/dx separation between other charged particles is also demonstrated.

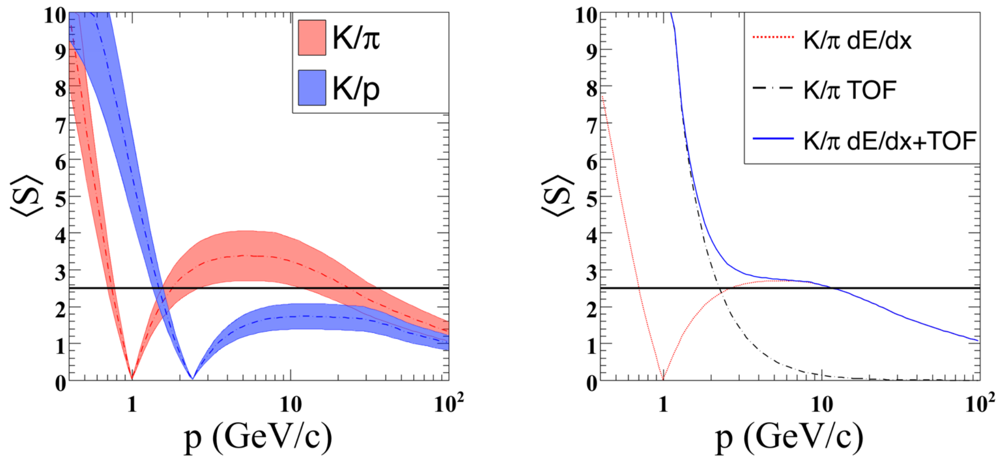

Figure 2.11: π-K separation performance at PICADOR detector. Left plot, dE/dx separation between different charged particles at $0.4 \sim 100$ GeV track momentum. Right plot, the separation power using both dE/dx and ToF information.

The difference between the dE/dx of pions and kaons vanishes at 1 GeV track momentum. Meanwhile, a significant portion of charged particle has energy smaller than 2 GeV at the CEPC. To separation these low energy charged particles, a Time of Flight (ToF) measurement with 50 ps time resolution is proposed. The ToF information could be measured by the ECAL, with a few layers equipped with the Time sensitive ASICs. Using both ToF and dE/dx information, a separation better than 2 σ could be achieved for tracks with momenta smaller than 20 GeV in the conservative scenario.

Considering the CEPC inclusive $Z \to q\bar{q}$ sample and integrate over the full polar angle and the momenta range of $2 \sim 20$ GeV, an over all charged kaon identification reaches an efficiency and purity of 91%/94% at the APODIS in the conservative scenario. If the dE/dx measurements could be improved to 3.6% (20% degrading comparing to the MCTruth), the efficiency and purity of charged Kaon identification could be improved to better than 95% **??**.

2.3.4 Photons

Successful photon reconstruction is crucial for the jet energy reconstruction, the $Br(H \rightarrow \gamma\gamma)$ measurement, and the physics measurements with τ leptons. Since the separation performance has been demonstrated in the section 2.2.2, this section is devoted to the reconstruction efficiency and the energy measurement of single photon.

The photon reconstruction is sensitive to the tracker material and the calorimeter geometry defects. To quantify their impact, a simplified, defect-free silicon tungsten ECAL geometry is implemented. This simplified geometry uses cylindrical barrel layer and its endcaps are directly attached to the barrel, forming a closed cylinder. The simplified geometry takes its inner radius and length of 1800 mm and 4700 mm (similar to the APODIS parameters). Along the longitudinal direction, the simplified ECAL is divided into 30 identical layers, each consist of one 2.8 mm tungsten absorber layer, one 0.5 mm silicon sensor layer and a 2 mm thick PCB layer. The thickness of the tungsten absorber and silicon sensor is adjustable, with which a dedicated optimization study has been performed and the ECAL geometry of APODIS is determined [**?**].

The reconstruction performance of a single photon is characterized by the finding efficiency and the energy collection efficiency. The finding efficiency is the chance that at least one ECAL cluster is reconstructed for one event with one photon incident into the detector fiducial region. The energy collection efficiency is defined as the accumulated hit energy in the photon cluster divided by that in all the hits.

At the simplified ECAL geometry, the finding efficiency reaches 100% for photons with energy larger than 500 MeV. The finding efficiency decreases to 85% once the photon energy is reduced to 100 MeV. The energy collection efficiency is better than 99% when the photon energy ranges from 1 GeV to 175 GeV. When the photon energy is less than 1 GeV, the energy collection efficiency degrades, i.e., the average energy collection efficiency decreases to 75% for 100 MeV photons. Since the simplified ECAL has no material before the calorimeter, it maintains high efficiencies even for low energy photons.

The single photon energy resolution of the simplified 30-layer ECAL is displayed as the black curve in Figure **??**, which is consistent with the test beam result of ILD ECAL prototype [**?**]. Reducing the number of layers (by enlarging the tungsten absorber thickness at each layer, but keep the) means fewer read-out channels, which leads to lower construction cost and power consumption. Keeping the total absorber thickness at the optimized value of 84 mm, reducing the readout layer numbers and maintaining the local sensor thickness, the ECAL energy resolution degrades as the sensor-absorber ratio decreases. Compared with 30 layers option, the energy resolution degrades by 11% at 25 layers and 26% at 20 layers.

The degradation of photon energy resolution by reducing the number of channels could be compensated by using thicker silicon sensor. We found that the energy resolution of ECAL at 20 layers with 1.5 mm thick silicon wafer, 25 layers with 1 mm thick wafer and the baseline geometry (30 layers with 0.5 mm thick wafer) has the same energy resolution. This conclusion is confirmed by the analyses at the Higgs physics benchmarks of $H \rightarrow \gamma\gamma$ and $H \rightarrow gg$ [**?**].

To conclude, the simplified geometry has an ideal efficiency of photon reconstruction and a consistent energy resolution w.r.t the CALICE ECAL prototype. We found that using thicker silicon wafer, the ECAL number of layers thus its construction cost and

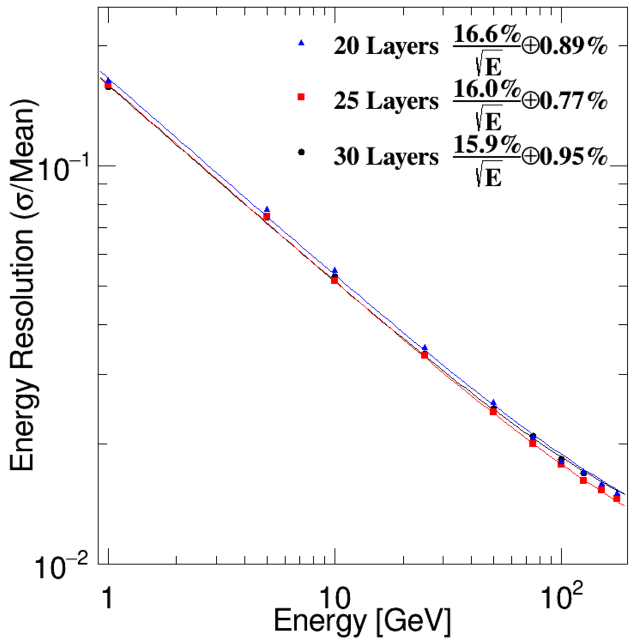

Figure 2.12: Energy resolution with fewer layers and thicker silicon wafers (20 layers with 1.5 mm silicon wafer and 25 layers with 1 mm silicon wafer), compared to 30 layers and 0.5 mm thick silicon wafer.

power consumption could be significantly reduced. Therefore, we strongly encourage the feasibility study of the thicker silicon sensor wafers.

At the APODIS detector, the total amount of material before the calorimeter is roughly 5-10$\%$ of one radiation length. This material will reduce the reconstruction efficiency for the low energy photons, and caused 5-10$\%$ of high energy photons to convert into electron-positron pairs. A preliminary converted photon finding algorithm is developed, with which 70$\%$ of the converted photon in $H \to \gamma\gamma$ events could be identified [**?**]. In addition, the geometry defects, such as the cracks between the ECAL modules, staves, and the dead zone between the ECAL barrel and endcaps, induces geometry based bias for the photon energy measurements and need to be corrected. The overall photon reconstruction could be benchmarked with the Higgs mass resolution at $H \to \gamma\gamma$ event at both simplified and the APODIS geometry, which will be discussed in section 2.3.4.1.

2.3.4.1 The di photon invariant mass distribution of vvH, $H \to \gamma\gamma$ events

The SM Higgs boson has 0.2$\%$ chance to decay into a pair of photons. Since photons could be easily identified, this channel becomes one of the Higgs discovery channels at the LHC. At the CEPC, this channel serves as a benchmark to characterize the ECAL performance.

Using the reconstructed $vvH, H \to \gamma\gamma$ sample and calculate the invariant mass of two most energetic photon candidates, we acquire the objective distributions at both simplified ECAL geometry and at APODIS, see Fig. 2.13 and **??**.

At the simplified ECAL geometry, a clean Gaussian distribution is identified with a tiny low mass tail. The low mass tail is induced by the artificial splitting of the photon cluster. A relative mass resolution of 1.7$\%$ is achieved, which agrees with the intrinsic electromagnetic energy resolution measured at the CALICE Si-W ECAL prototype test beam experiments [**?**].

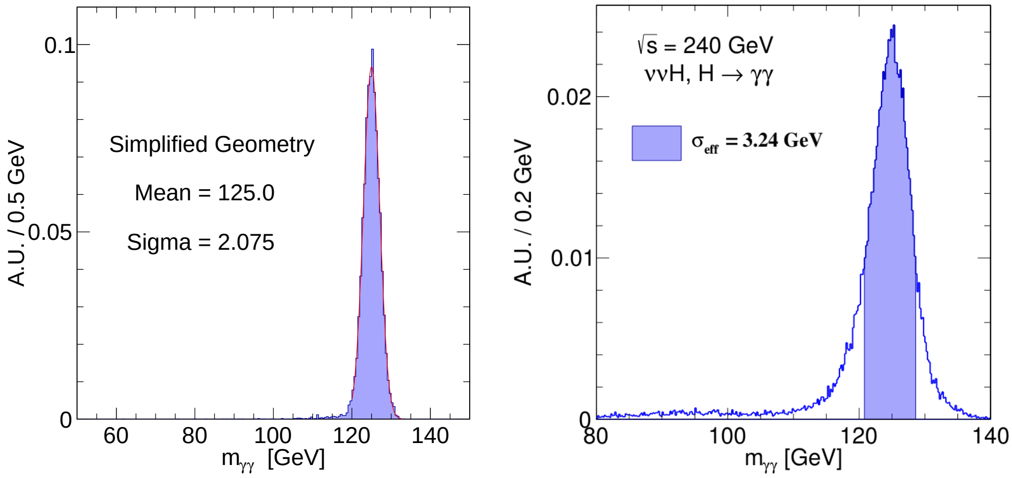

Figure 2.13: The reconstructed Higgs invariant mass of $H \to \gamma\gamma$ events at the simplified detector geometry (Left) and at APODIS (Right). 10k and 6k events are reconstructed correspondingly. Each distribution is normalized to unit area.

Comparing to the simplified geometry, the relative resolution of the Higgs mass at APODIS degrades significantly. A preliminary geometry based correction algorithm has been developed, which scales the energy of EM clusters located at the geometry cracks. This distribution could be fit to a core Gaussian center and a wider Gaussian with a lower mean value. The core gaussian exhibits a mass resolution of 1.9%, while the low-mass wider gaussian is caused by the fact that the correction algorithm is only optimized. The average mass resolution (taking a weighted average of both Gaussian) is then 2.3%. The latter can be improved with much dedicated correction algorithm.

To summarize, our simulation predicts the Higgs mass resolution at two-photon final state reaches 1.6-2.3% level at the CEPC. This result is consistent with the CALICE prototype test beam result. The reconstruction of converted photons and the correction of the geometry defects at any realistic detector geometry is crucial for the photon reconstruction.

2.3.5 Jet

The jet is fundamental for the CEPC physics program. About 90% of the SM Higgs boson decays into final states with jets (70% directly to di-jet final states; and roughly 20% via decay cascade from the ZZ^*, WW^*), while 70% of W and Z bosons decay into di-jet final states. Roughly 60% of the jet energy is carried by the charged particles, and the Particle Flow could improve significantly the precision of jet energy measurement with respect to the calorimeter based reconstruction.

In the Particle Flow reconstruction, the jet candidates are constructed from the reconstructed final state particles via the jet clustering algorithms. The ambiguity from the jet clustering is significant and usually dominants the uncertainty, especially for these events with more than two final state jets such as the measurement of $g(Hb\bar{b})$, $g(Hc\bar{c})$, and $g(Hgg)$ via $ZH \to 4jet$ events.

To characterize the jet reconstruction performance, a two-stage evaluation has been applied at the CEPC studies. The first stage is the Boson Mass Resolution (BMR) analysis designed to avoid the complexity induced by the jet clustering. The second is the individual jet response analysis, which requests the jet clustering.

The Boson Mass Resolution analysis is applied to physics events with two final state jets decayed mostly from one intermediate gauge boson, including

1, $\nu\tilde{\nu}q\bar{q}$ events via the ZZ intermediate state;

2, $l\nu q\bar{q}$ events via mostly WW intermediate state;

3, $\nu\tilde{\nu}H$ events with $H \to b\bar{b}, c\bar{c},$ or gg.

In these processes, besides the jet final state particles, the other particles are either invisible or could be easily identified. The invariant mass of all the final state particles decayed from a massive boson can therefore be reconstructed. Therefore, disentangled from the jet clustering algorithm, the BMR evaluates the jet reconstruction. Meanwhile, the BMR shows immediately how these massive gauge bosons can be separated at jet final state.

Using the jet clustering and matching algorithms, the jet response is also analyzed at each individual jet. The overall response includes the detector resolution, the ambiguous induced by the jet clustering and the mismatching. These effects are physics process dependent and a complete analysis is beyond the scope of this manuscript. In this paper, this analysis is limited to individual jet reconstruction performance at $\nu\tilde{\nu}q\bar{q}$ process.

Corresponding to 5 ab^{-1} integrated luminosity at the CEPC, we simulate 1.8 millions $\nu\tilde{\nu}q\bar{q}$, 11 millions $l\nu q\bar{q}$ and 170 thousands $\nu\tilde{\nu}H, H \to jj$ events at $\sqrt{s} = 250\ GeV$ with the CEPC v_1 geometry. All these samples are reconstructed with Arbor. Fig. 2.14 shows the inclusive reconstructed boson mass distributions normalized to unit area. These distributions are well separated, each exhibits a peak at the expected boson mass. These mass distributions are all asymmetric for different reasons. At the low mass side, the green distribution, corresponding to $\nu\tilde{\nu}H, H \to jj$ events, has a long tail. This tail is mainly stemmed from the neutrinos generated in the heavy jets fragments (most of the $H \to jj$ events are $H \to b\bar{b}$ events). The heavy jet components are also responsible for the low mass tail in the other two distributions. Because W boson hardly decays into b-jets, the low mass tail of $l\nu q\bar{q}$ sample is much less significant. The Breit-Wigner width of massive gauge bosons and the phase space effects also contribute to the long tails at the $l\nu q\bar{q}$ and the $\nu\tilde{\nu}q\bar{q}$ samples. The high mass tail induced by ISR photon(s) is observed in each distribution.

To decouple the detector response from these physics effects, a standard cleaning procedure is designed:

1, The jets are generated from light flavor quarks (u, d) or gluons.

2, Acceptance: the partons should have a significant angle to the beam pipe: $|cos(\theta)| < 0.85$.

3, ISR veto: there is no energetic visible final state ISR photon: the accumulated scalar transverse momentum of the ISR photons should be smaller than 1 GeV.

4, Neutrino veto: there is no energetic neutrino generated from the jet fragmentation cascade: the accumulated scalar transverse momentum of the jet neutrinos should be smaller than 1 GeV.

This event selection clearly leads to narrow boson mass distribution and better separation, see Fig. **??**.

After this event selection, the mass distributions are much symmetric. The Higgs boson mass could be simply fit to a Gaussian, while the other two distributions include the non-negligible intrinsic widths. The efficiency of this event selection depends on the decay branching ratio (condition 1), differential cross section (condition 2), the radiation behavior (condition 3) and jet fragmentation (condition 4). As in the $\nu\tilde{\nu}H, H \rightarrow gg$ sample, this event selection has an overall efficiency of 65% (75%/94%/94% for the 2nd/3rd/4th condition, respectively). The relative mass resolution of the Higgs mass is then 3.8%, providing a quantitative reference for the BMR.

It should be remarked that both lepton identification and jet flavor tagging information are available in current reconstruction. Combing these information enhances the distinguishing power on different physics processes.

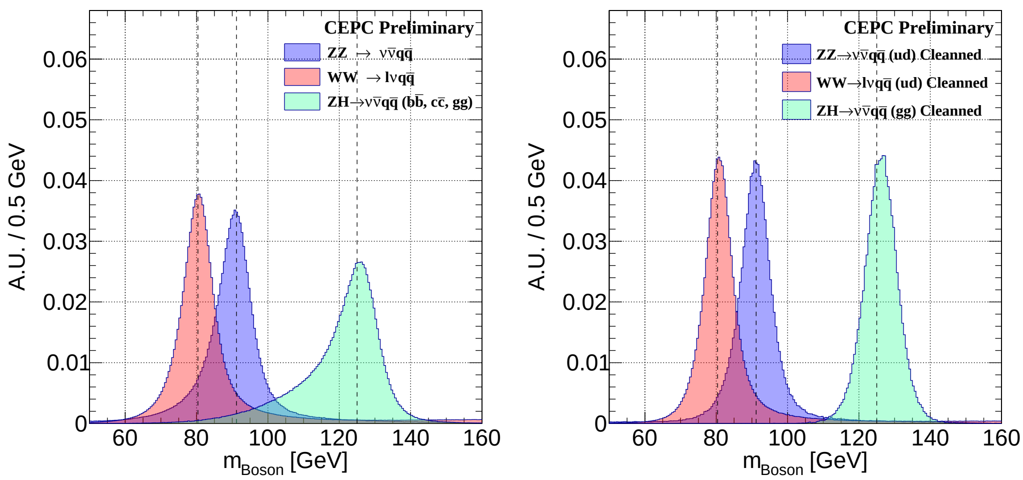

Figure 2.14: Reconstructed boson masses of the inclusive (Left) and cleaned (Right) $l\nu q\bar{q}$ (red), $\nu\tilde{\nu}q\bar{q}$ (blue) and $\nu\tilde{\nu}H, H \rightarrow jj$ samples (green).

The calibration process plays an important role in measuring the jet energy. Technically, Arbor was calibrated via two steps, the single particle level calibration, and the data-driven calibration. The single particle calibration is to figure out the global ECAL/HCAL calibration constants according to the comparison between the reconstructed neutral particle energy and the truth. The ECAL calibration constant is derived from photon samples while the HCAL calibration constant at K_L^0 samples. Due to the Particle Flow double counting, i.e. the fragments of charged particle showers are misidentified as neutral particles, the single particle calibration leads to typically 1% overestimation on the boson mass. The data-driven calibration is to scale all the reconstructed boson masses according to the W mass peak exhibited in the $l\nu q\bar{q}$ events, the leading physics processes of the above three. This simple calibration simultaneously scales the three boson mass peak positions to the expected positions. To fully appreciate the enormous productivity of massive bosons at the CEPC, sophisticated calibration methods must be developed and validated for the real experiments, i.e. control and corrections of differential dependences, in-situ calibrations, detector homogeneity monitoring and control, *etc*.

The reconstruction performance of individual jet is explored via the same $\nu\tilde{\nu}q\bar{q}$ sample. Using ee-anti-kt algorithm (a.k.a Durham algorithm [**?**]), all the reconstructed particles are forced into two jets (recojets). The same jet-clustering algorithm is applied to the visible final state particles at the MC truth level, forming the generator level jets (genjets). Using a matching algorithm that minimizes the angular difference, the jet reconstruction performance is characterized by the difference between the 4-momentum of the initial quarks, the genjets, and the recojets. The difference between the quarks and the genjets is mainly coming from the fragmentation and the jet clustering processes, while the difference between the genjets and the recojets is induced by the jet clustering, matching, and the detector response. A dedicated analysis shows that, even at this simple di-jet process, the uncertainty induced by the jet clustering and matching can be as significant as those from the detector response [**?**].

These two reconstructed jets are classified into leading/sub-leading jets according to their energy. The relative energy difference between genjet and recojet is then fit with a double-sided crystal ball function. The exponential tails are mainly induced by the jet clustering algorithm, the matching performance, and the detector acceptance. The Gaussian core then describes the detector resolution, therefore we define its mean value as the Jet Energy Scale (JES) and its relative width as the Jet Energy Resolution (JER).

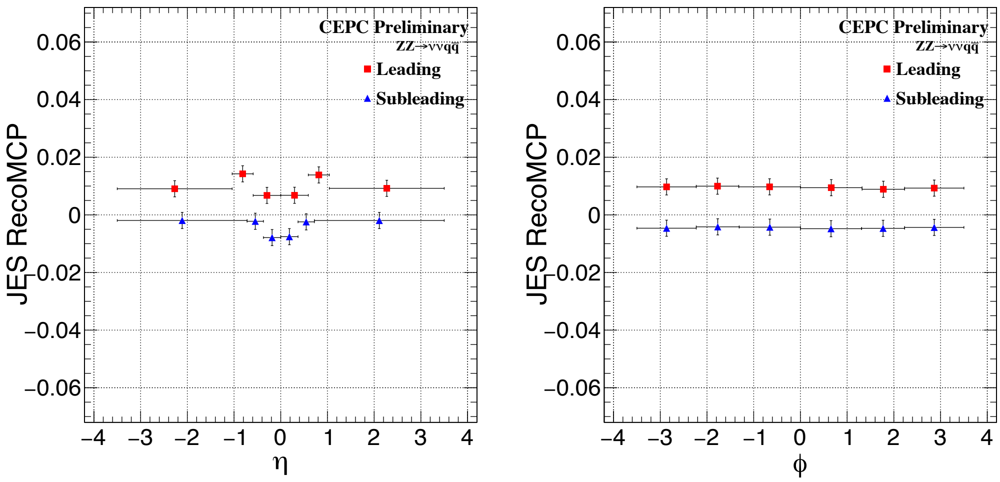

Figure 2.15: Jet energy scale at different jet directions.

Fig. 2.15 shows the JES at different jet directions. The JES is flat along the azimuth angle. Along the polar angle, the JES increases significantly for the leading jets in the overlap part between the endcap and the barrel. The JES is also larger in the endcap than in the barrel. These patterns are correlated with the Particle Flow confusions, especially the artificial splitting of the charged clusters. Not surprisingly, the leading jets have a systematically higher JES comparing to the sub-leading one. Without any corrections, the entire amplitude of the JES is controlled to 1% level, which is significantly better than that of LHC even after the correction [**?**].

The jet energy resolution (JER) at different jet transverse momenta is displayed in Fig. 2.16. The overall JER takes a value between 6% (at $P_t < 20$ GeV) to 3% (at $P_t > 100$

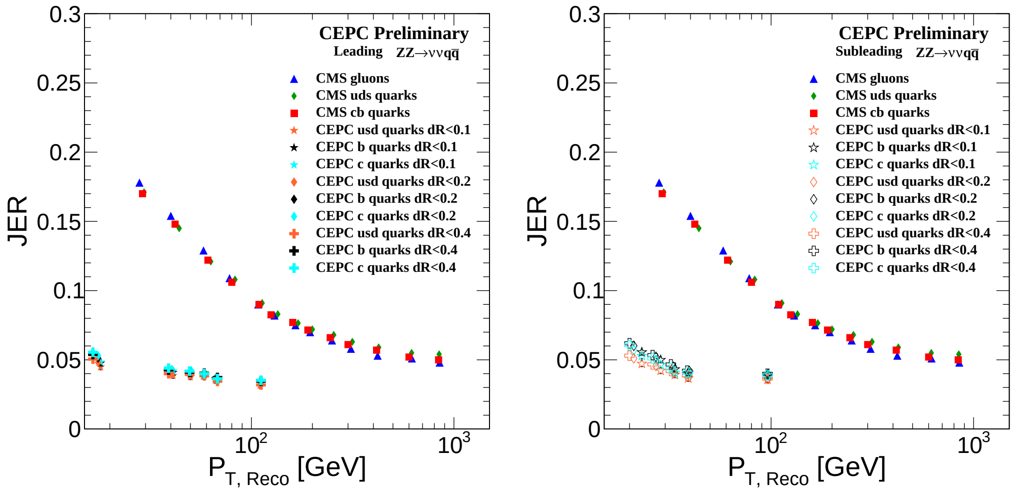

Figure 2.16: The jet energy resolution for leading (upper) and sub-leading jets (lower), as a function of the jet transverse momenta. The performance at the CMS [**?**] has been overlapped for comparison.

GeV). The leading jets usually has a slightly better JER comparing to the sub-leading ones. Taking the performance of the CMS detector as a reference, the JER at the CEPC reference detector is 2-4 times better at the same P_t range [**?**].

To conclude, the jet energy response has been analyzed at the BMR level and at the individual jet level. For physics events with only two jets, the boson mass could be measured to a relative accuracy better than 4% at CEPC v_1 using a standard event selection. This resolution ensures significant separation between the W boson, the Z boson, and the Higgs boson. At individual jets, the JES is controlled to 1% level and the JER of 3% to 6%, both are significantly better than the LHC detector performances. This superior performance is based on the clean electron-positron collision environment, the PFA oriented detector design and reconstruction. It is highly appreciated for the CEPC physics program, i.e. the measurements of W boson mass at the CEPC Higgs operation. It should also be emphasized that the jet-clustering algorithm has a strong and even dominant impact on the physics measurements with multiple jets in the final states. Tested at the $\nu\tilde{\nu}H, H \to jj$ events, the APODIS detector model gives the same jet energy resolution.

2.3.5.1 Total visible mass distribution of $H \to bb, cc, gg$ events

The majority of the SM Higgs boson decay into di-jet final states: 58%/3% into a pair of b/c quarks via the direct Yukawa coupling, and 8% into a pair of gluon mainly via top quark loop. These di-jet events could be easily identified using its invariant masses. The jet performance has been intensively discussed in section **??**, where the inclusive invariant mass distribution of $vvH, H \to di - jets$ and a cleaned distribution of $vvH, H \to gg$ are both presented. In this section, we are going to show all these 6 distributions of $vvH, H \to bb, cc, gg$ wi/wo cleaning.

These inclusive distributions (Fig. 2.17) clearly exhibit nongaussian, asymmetric patterns. As discussed in section **??**, these patterns are induced from visible ISR photons, neutrinos generated in Higgs decay cascade, and the detector acceptance. Applying the corresponding cuts in the standard cleaning procedure (defined in section **??**), these patterns disappear, see Fig. **??**.

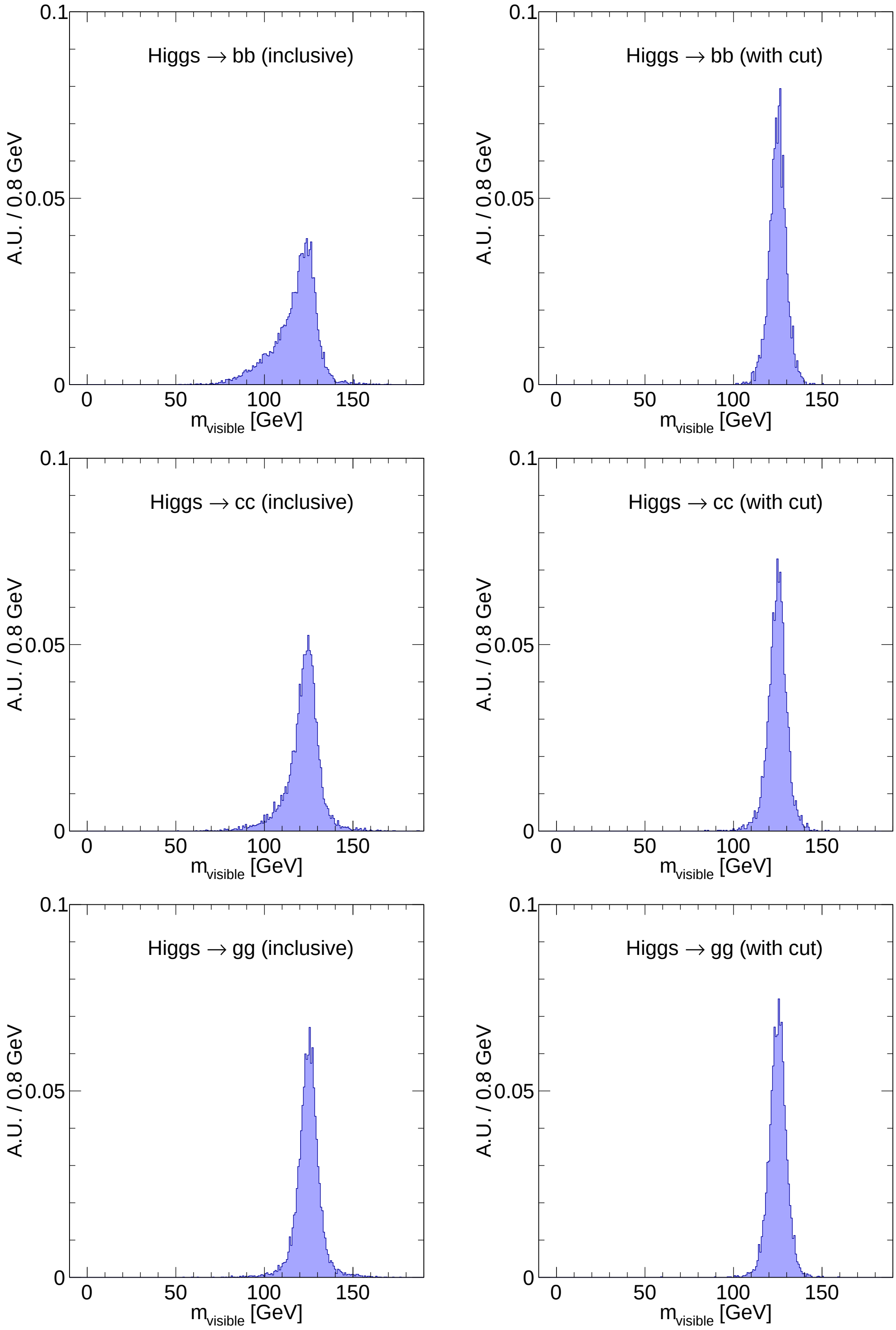

Figure 2.17: Total visible mass distribution of $vvH, H \to di-jet$ events, with/without cleaning

-	$H \to bb$	$H \to cc$	$H \to gg$
Sample statistic	10k	10k	9.6k
$\epsilon_{ISRveto}$	94%	94%	94%
$\epsilon_{neutrinoveto}$	41%	69%	94%
$\epsilon_{acceptance}$	74%	74%	74%
Relative mass resolution	$3.60 \pm 0.07\%$	$3.76 \pm 0.05\%$	$3.69 \pm 0.04\%$

Table 2.2: Statistics, cut efficiencies on the $vvH, H \to dijet$ samples and the relative mass resolution after the cleaning.

The corresponding efficiencies and statistics are summarized in Table 2.2. For three different decay modes, the neutrino veto condition has different efficiencies, and vetoed more than half of the $H \to bb$ events. The other two condition have essentially identical efficiencies. After the cleaning, the relative mass resolution for three different decay modes converge to a similar level.

2.3.5.2 Total visible mass distribution of $H \to WW^*$ and ZZ^* events

The Higgs boson have large couplings to the massive gauge mediator. It has a branching ratio of 21%/3% to decays into a pair of W/Z boson, respectively. Limited by the Higgs mass, only one of the massive gauge boson is on shell. The total visible mass for the $vvH, H \to WW^*/ZZ^*$ events are shown in Fig. 2.18.

The cascade decay of $H \to ZZ^* \to 4l$ is the other Higgs discovery channel at the LHC, as multiple leptons is a clean signature. At the CEPC, combining the $Br(H \to ZZ^*)$ measurements and the g_{HZZ} measurements via the recoil mass methods leads to a direct, model independent determination of Higgs total width, therefore this measurement is of strong physics interests. The $Br(H \to WW^*)$ also a gateway measurement to the absolute Higgs width measurement. In addition, the large statistic of $H \to WW^*$ events makes it a sensitive probe to the new physics.

Both W and Z bosons decays into SM fermions except the top quarks. Therefore, a successful reconstruction of the $Br(H \to WW^*/ZZ^*)$ signal requires a proper reconstruction of leptons, taus, missing energy and jets.

The $H \to WW^*$ events could cascade decay into hadronic, semi-leptonic, and full-leptonic final states. The mass distributions corresponding to different decay modes are separated in the left hand plot of Fig. 2.18. A full mass peak, corresponding to the full-hadronic final states, could be clearly identified.

Four peaks could be identified at the distribution of $Br(H \to ZZ^*)$. The peak at zero corresponding to the total invisible decay mode where both Z and Z* decays into neutrinos and has a branching ratio of roughly 4%. The peak at the Higgs boson mass (125 GeV) is corresponding to the total visible mode. The other two peaks are corresponding to the conjugation case where $Z \to visible, Z^* \to invisible$ and $Z^* \to visible, Z \to visible$. Because of the heavy flavor and τ component of the Z boson decay, the peak at 125 GeV and at the Z boson mass exhibit a tail at the low mass side. For both $H \to WW^*$ and

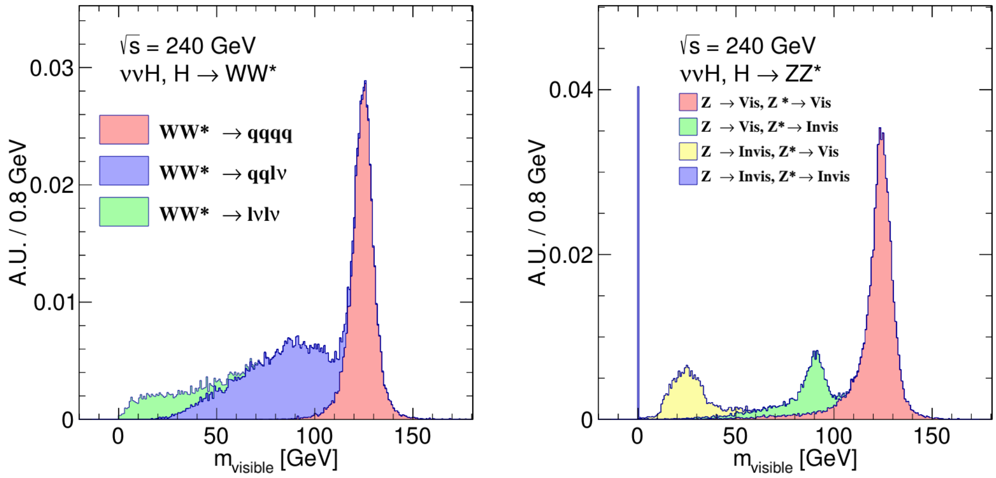

Figure 2.18: Total visible mass distribution of $H \to WW^*$ (Left) and $H \to ZZ^*$ events (right).

$H \to ZZ^*$ final states, a relative mass resolution of 3.8% is achieved with the full visible peak, which is consistent with the results at $H \to 2jets$ final states.

Fig. **??** exhibits beautiful separations of different components of $H \to ZZ^*$ events, those clear signature is highly appreciated in the physics measurements. In fact, using only the conjugating events where the $H \to ZZ^*$ signal decays into $llvvqq$ final states, a relative accuracy of 5% on the $Br(H \to ZZ^*)$ measurement could be achieved [**?**]. The statistic uncertainty of $Br(H \to WW^*)$ measurement should be controlled well below 1%.

2.3.6 Jet flavor tagging

Identification of the jet flavor is essentially for the measurement of the Higgs couplings ($g(Hb\bar{b}), g(Hc\bar{c}), g(Hgg)$) and the EW observables at the CEPC. During the jet fragmentation cascade, the heavy flavor quarks (b and c) are mostly fragmented into heavy hadrons (i.e. B^0, $B^{\pm}$, B_s, D^0, $D^{\pm}$, *etc*). Those heavy hadrons have a typical $c\tau$ of a few hundred micrometers. Therefore, the reconstruction of the secondary vertex is crucial for the flavor tagging. The information of jet mass, vertex mass, number of leptons, *etc*, are also frequently used in flavor tagging.

Technically, the flavor tagging is operated using the LCFIPlus package [**?**], the default flavor tagging algorithm for the linear collider studies. At CEPC studies, the LCFIPlus takes the reconstructed final state particles from Arbor, reconstructs the second vertexes and performs the flavor tagging. For each jet, LCFIPlus extracts more than 60 distinguish observables and calculates the corresponding b-likeness and c-likeness using the Boost Decision Tree method [**?**]. Since the b-mesons have longer lifetime compared to the c-mesons, the c-tagging is much more challenging than the b-tagging. Thanks to the high precision vertex system, the c-jet could be distinguished from other jets at the ILD detector and the CEPC v_1 detector. Fig. 2.19 shows the reference ROC curve trained on $Z \to q\bar{q}$ sample at 91.2 GeV center of mass energy. The X-axis indicates the b/c-jet efficiency, while the Y-axis represents the surviving rate for the backgrounds.

Applying to the inclusive $Z \to q\bar{q}$ sample, the typical performance of the b-tagging reaches an efficiency/purity of 80%/90%, changing the working point to a reduced effi-

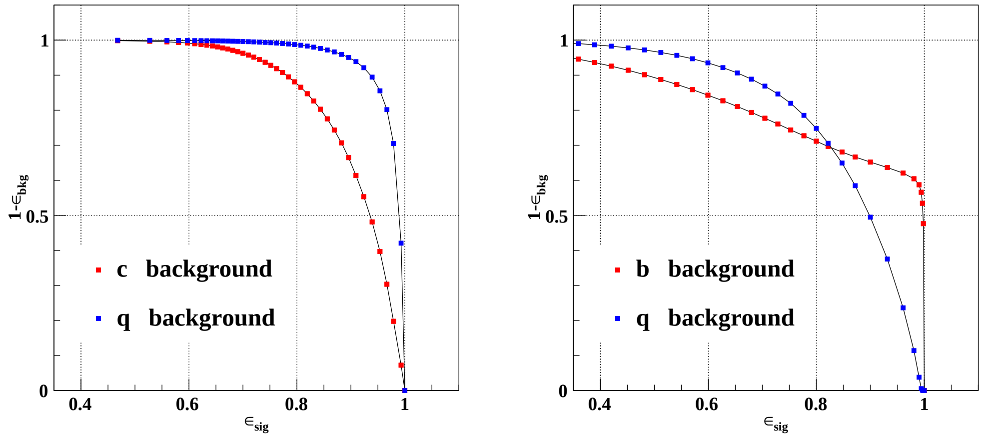

Figure 2.19: The jet flavor tagging performance using Arbor and LCFIPlus reconstruction at APODIS.

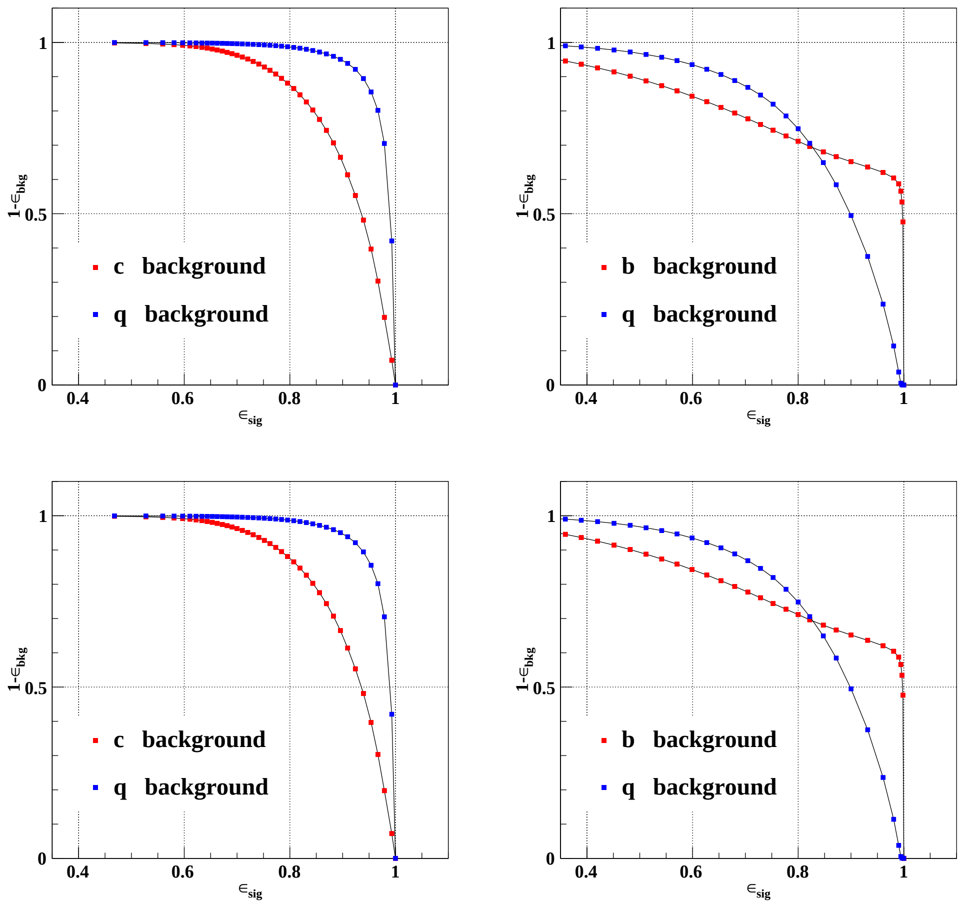

Figure 2.20: The heavy flavor jet likelihood for Higgs samples: a, $H \to bb$; b $H \to cc$; c, $H \to gg$, and d, $H \to 2jets$

ciency of 60%, the purity could be enhanced close to 100%. While for c-tagging, a typical working point has the efficiency/purity of 60%/60%.

The distribution on the phase space for $H \rightarrow 2jets$ samples are displayed in Fig. 2.20. Depending on the Higgs decay final states, those distributions clearly exhibits different patterns. It should be emphasized that, with the current detector geometry design and reconstruction algorithm, the c-tagging is still very difficult. As a result, the accuracy of $g(Hc\bar{c})$ measurement is largely limited by the contamination from the $H \rightarrow b\bar{b}$ events.

2.4 conclusion

Targeting at precise measurements of the Higgs boson properties and the EW observables, the CEPC detector is required to reconstruct all the corresponding physics objects at high efficiency and high accuracy. The performance of the baseline detector design, the APODIS, has been intensively analyzed at full simulation level. The following object level performances have been achieved.

1, Lepton identification: $\epsilon_{e\rightarrow e} > 99.5\%$, $\epsilon_{\mu\rightarrow\mu} > 99.5\%$, $P_{h\rightarrow lepton} < 1\%$ for isolated tracks with energy larger than 2 GeV;

2, Charged Kaon identification: efficiency/purity of 95%/95% at inclusive Z pole sample with the energy range of 2 - 20 GeV;

3, Photon reconstruction: a relative accuracy of 1.7%/2.6% is achieved for the Higgs mass reconstruction at $H \rightarrow \gamma\gamma$ event using simplified/APODIS detector geometry;

5, Jet energy resolution: A relative accuracy of 3.8% of Boson mass reconstruction is achieved at a cleaned $H \rightarrow gg$ event sample. The Higgs boson, the Z boson, and the W boson can be efficiently separated from each other in their hadronic decay modes. The jet energy scale is controlled to 1% level. At individual jet, the relative jet energy varies from 3% to 6%, depending on the jet transverse momentum.

6, Jet Flavor Tagging: at the inclusive $Z \rightarrow q\bar{q}$ samples at 91.2 GeV, the b-jets could be identified with an efficiency/purity of 80%/90%; while the c-jets could be identified with efficiency/purity of 60%/60%.

Essentially, all the physics objects are successfully reconstructed by the CEPC baseline. The performances at the single particle level, such as the leptons, the kaons, and the photons at simplified geometry, are close to the physics and/or hardware limits. The separation and high-efficiency reconstruction of charged particles/photons ensure good τ lepton reconstruction. The jet energy resolution leads to a clear separation between massive bosons at di-jet events. The LCFIPlus algorithm could then distinguish b-jet, c-jet, and light-jet from each other.

A comprehensive analysis of the Higgs signal distributions shows that the SM Higgs signals are well established and have clean signatures. Based on the APODIS detector design, we characterize the Higgs signatures at the $e^+e^- \rightarrow \nu\nu Higgs$ events. The detector resolution could then be directly characterized by the mass resolution with Higgs $\rightarrow \mu\mu, \gamma\gamma$, and jet final states. Comparing to the LHC, the reconstruction accuracy at Higgs $\rightarrow$ $\mu\mu$ events is improved by about one magnitude, and that at Higgs $\rightarrow$ di-jets

	Higgs$\rightarrow\mu\mu$	Higgs$\rightarrow\gamma\gamma$	Higgs$\rightarrow$bb
CEPC (APODIS)	0.20%	2.59%	3.63%
LHC (CMS, ATLAS)	~2% [**?** **?**]	~1.5% [**?** **?**]	~10% [**?** **?**]

Table 2.3: Higgs boson mass resolution ($\sigma/Mean$) at different decay modes with jets as final state particles, after the event cleaning

events is improved by about 3 times. The resolution at Higgs $\rightarrow\gamma\gamma$ events degrades by roughly 30-60%, limited by the absence of geometry based correction and fine-tuned calibration, and the sampling fraction of ECAL, see Table 2.3.

To conclude, the baseline design fulfills the physics requirements discussed in Chapter 3.

References

[1] M. Ruan, *Shower fractal dimension analysis in a highly-granular calorimeter*, Journal of Physics: Conference Series **490** (2014) no. 1, 012227. `http://stacks.iop.org/1742-6596/490/i=1/a=012227`.

[2] D. Yu, M. Ruan, V. Boudry, and H. Videau, *Lepton identification at particle flow oriented detector for the future e^+e^- Higgs factories*, Eur. Phys. J. **C77** (2017) no. 9, 591, `arXiv:1701.07542 [physics.ins-det]`.

./

CHAPTER 3

PHYSICS POTENTIAL

3.1 Introduction

The CEPC produces huge statistics of massive SM Bosons. Its physics potential is explored on three different classes of physics benchmarks, the Higgs physics, the precision EW physics, and the flavor physics. Using the software tools introduced in Chapter **??**, the physics potential on Higgs physics is analyzed at full simulation level, see section 3.2. The accuracies on the EW precision measurements are mainly limited by systematic errors and are estimated in section **??**. Being a powerful Z factory, the CEPC also has prominent potential on the flavor physics, which has been analyzed in section **??**. The synergies of these different physics measurements, the complimentary and comparison to the HL-LHC and other high energy physics programs are discussed in section **??**.

3.2 Higgs physics

The core of the entire CEPC physics program is the production of 1 million Higgs bosons. Three different kinds of the Higgs measurements can be performed.

The first class is the recoil mass analyses, see section 3.2.1. Most of the Higgs bosons at the CEPC is produced through the Higgsstrahlung events. Knowing precisely the initial state and measuring the 4 momentum of the Z boson, the 4 momentum of the Higgs boson could be determined. In other word, the Higgs signal could be identified without using the Higgs decay information, and therefore the inclusive cross section of Higgsstrahlung events could be measured, leads to a model independent measurement of $g(Hzz)$. This recoil mass analysis also gives excellent access to the exotic Higgs decay modes. Meanwhile, the Higgs mass could be measured directly from the recoil mass distribution.

The second class is the Higgs event rate measurements. Similar to the LHC, the Higgs events with different generation modes and decay modes could be identified, leading to the measurement of corresponding event rates. These event rates, once combined with the measurement of $g(Hzz)$, could derive the absolute value of the Higgs branching ratio, the Higgs total width, and the couplings between the Higgs bosons and its decay final states. On the other hand, almost all the Higgs decay modes with branching ratio larger than 10^{-4} could be identified at the CEPC. An inclusive description of the event rate measurements is summarized in section 3.2.2.

The third one is the differential Higgs measurements, see section 3.2.3. The clean collision environment of the electron positron collider and the excellent angular resolution of the detector leads to a precise measurement of the differential distributions on the physics events. In terms of the Higgs physics, these differential measurements are highly appreciated in the determination of the Higgs boson quantum numbers, and the measurements of Effective Lagrangian Theories.

...

3.2.1 Recoil mass analyses

The recoil analysis via $\mu^+\mu^-H$ channel is one of the most characteristic measurements of the CEPC Higgs program. It determines both Higgs mass and the absolute value of $\sigma(ZH)$, which in turn anchors all the absolute Higgs measurements. The essence of this measurement is to use only the information from di-muon system. Therefore, the biases from the Higgs decay modes can be excluded. All the SM processes with one pair of reconstructed muons - which may also come from misidentification - are the background.

As an important physics benchmark this recoil mass analysis has been iterated with different detector models and setups. In this section, we will first present in details the analysis at PreCDR set up, where the detector geometry is CEPC v_1 and at the center of mass energy is at 250 GeV. and then present the result with CDR set up (using APODIS detector geometry and at 240 GeV center of mass energy). A comparison and discussion can be found at the end of this section.

Corresponding to 5 ab^{-1} integrated luminosity, a Higgs signal sample has been fully simulated and reconstructed according to the PreCDR setup. Limited by the computing resource, a pre-selection is applied and only a fraction of the entire SM background are processed with full simulation. This pre-selection relies on the information of the di-lepton system:

1, For each muon candidate, the energy is requested to be larger than 20 GeV;

2, the total invariant mass of the muon system is close to the mass of Z boson: $|m_{ll} - 91.2| < 20$.

This pre-selection efficiently reduces the inclusive SM background by four orders of magnitudes. In fact, the leading SM background after this event selection is mainly the irreducible background of $ZZ \to \mu^+\mu^- + X$, and $WW \to \mu^+\mu^-\nu\nu$. The $\mu^+\mu^-\nu\nu$ background can be vetoed by requesting visible signal at the recoil side of the muon system, since the SM Higgs signal mostly decays visibly. As this veto cut uses the Higgs decay information, it's not applied in the model independent measurement of $\sigma(ZH)$ but only used for the Higgs mass measurement.

	$\mu\mu H$	SM backgrounds
Total events	35247	655659715
pre-selection	97.7%	0.26%
$120\ GeV < M_{recoil} < 150\ GeV$	93.2%	0.19%
$80\ GeV < M_{inv} < 100\ GeV$	85.5%	0.03%
$P_{T_{\mu\mu}} > 20\ GeV$	80.2%	0.013%
$\Delta\phi < 175°$	77.8%	0.008%

Table 3.1: Cut chain and efficiencies of signal and background for $\mu\mu H$ channel.

The event selection at the reconstructed data sample has two steps. The first step is the recovery of pre-Cuts with stricter cuts, and the second step is to use other kinematic information such as P_t balance condition and lepton system polar angle. The first step requires:

1, For each muon candidate, the energy is requested to be larger than 25 GeV;

2, the total invariant mass of the muon system is close to the mass of Z boson: $|m_{ll} - 91.2| < 10$.

Comparing to the detector resolution, the recovery conditions are sufficiently stricter than the pre-selection. A complete cut chain is presented in Table. 3.1. The main background after the selection is the ZZ background.

After the event selection, the final plot is shown in Fig. 3.1.

The signal essentially could be fit to a double sided crystal ball function. The background is smooth and can be described by a third order polynomial function, see Fig. 3.1. Based on the fit results, σ_{ZH} could be measured to a relative precision of 0.85%. Meanwhile, fitting the peaking position of the signal leads to a Higgs mass measurement with precision of 6.5 MeV (the model independent analysis). Imposing information measured from Higgs decay side, the mass resolution could be improved to 5.4 MeV (the model dependent analysis).

Following the same procedure, the same analysis has been re-performed at the APODIS geometry with 240 GeV center of mass energy (the CDR setup), see Fig. **??**. The results are summarized in Table. 3.2. Once the center of mass energy is reduced from 250 GeV to 250 GeV, the cross section of the signal is reduced by 5% and that for the background increased by 4%. In terms of the detector performance, both setups has a same event reconstruction efficiency of 97% (defined by the probability of finding a pair of muons in the reconstructed particle list), while the momentum resolution at the CDR setup degrades by 15% comparing to the PreCDR setup, proportional to the solenoid B-Fields strength. Comparing to the PreCDR setup, the height of the Higgs mass peak at the CDR setup decreased by 20%, as a result of the degrading of B-Field (15%) and the change of physics cross-sections, and the Higgs mass resolution degrades by 7%. The accuracy on the $\sigma(ZH)$ measurements is less sensitive to the degrading of the center solenoid B-Field, and a relative degrading of 5% is observed.

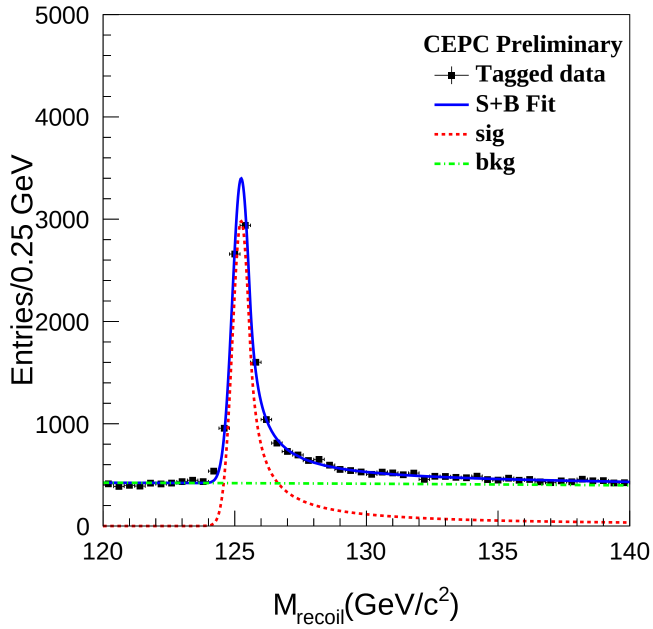

Figure 3.1: Higgs recoil mass distribution after the Event Selection with CEPC-v1 geometry at 250 GeV center of mass energy.

	CEPC v_1	APODIS
$\sqrt{s}/GeV$	250	240
$\int Ldt/ab^{-1}$	5	5
$\delta m_H/MeV$ (M-I)	6.5	6.9
$\delta m_H/MeV$ (M-D)	5.4	5.9
$\delta\sigma_{ZH}/\sigma_{ZH}$	0.81%	0.85%

Table 3.2: Comparison of accuracies on $\sigma(ZH)$ and Higgs mass with the CDR setup and the PreCDR setup. The accuracies on Higgs mass measurements are estimated with both Model independent analysis (M-I) and Model dependent analysis (M-D).

3.2.2 Measurements of Higgs event rates

3.2.2.1 Measurement of $\sigma(ZH) \times Br(H \to \tau^+\tau^-)$

A significant fraction of the SM Higgs boson decays into $\tau^+\tau^-$ final state. Meanwhile, the third generation fermions are sensitive to the new physics. That's why the measurement of $\sigma(ZH) * Br(H \to \tau^+\tau^-)$ provides a sensitive New Physics probe. On the other hand, the τ lepton has various different decay modes. The τ leptons decayed from the Higgs boson are significantly boosted, leading to a narrow jet composed of potentially multiple visible final state particles. Therefore, this benchmark analysis becomes a test bed for the detector performance, especially for the separation performance emphasized by the Particle Flow principle.

A full simulation analysis on this measurement is performed at Ref. [**?**]. Corresponding to $5ab^{-1}$ integrated luminosity and the PreCDR setup (250 GeV center of mass energy and the CEPC v_1 geometry model), a SM sample is generated. In this analysis, the Higgs signals are classified into sub-channels of $\mu^+\mu^-H$, e^+e^-H, vvH and qqH processes and analyzed independently.

According to the number of the final state jets, the Higgs signals are classified into the hadronic and the leptonic type, represented by the $\mu^+\mu^-H$ and qqH processes respectively. We are going to briefly summarize these two sub-channel analyses in section 3.2.2.2 and 3.2.2.3, respectively. Same analyses are also performed at the CDR setup (240 GeV center of mass energy with the APODIS detector geometry), a comparison of the results is presented and discussed in section 3.2.2.4.

3.2.2.2 The leptonic channel: $\mu^+\mu^-H, H \to \tau^+\tau^-$

In this channel, the signal signature includes the invariant and recoil mass of the initial muon pairs, and the finite multiplicity of charged particles and photons decay from τ leptons.

Using the known Z boson mass, the initial muon pair can be identified and the remaining particles are hypothesized to be the $\tau^+\tau^-$ system. The first step of the event selection composed of the restrictions on the invariant/recoil mass of the $\mu^+\mu^-$ system, and the multiplicity of the hypothesized $\tau^+\tau^-$ system. Shown in Ref. [**?**], these conditions kept a signal efficiency of 98% and reduced the inclusive SM background by three orders of magnitudes. The leading remaining backgrounds are the irreducible Higgs backgrounds (i.e. $H \to WW^*, ZZ^* \to \tau^+\tau^-\nu\tilde{\nu}$) and the ZZ backgrounds with the same final states.

Further event selection has been made on a TMVA combination of the multiplicity of the $\tau^+\tau^-$ system and the distances between particles. Table **??** shows the cut chain of this channel.

Thanks to the PFA oriented design and reconstruction, the final event selection reduced the inclusive SM background by nearly six orders of magnitudes, while preserves a signal efficiency of 93%. In addition, giving the significant cτ of the τ lepton (89 μm) and the precise vertex system at APODIS, the signal and background could be further separated using the track impact parameter D_0 and Z_0. For each track, we define a pull parameter as $(D_0)^2 + (Z_0)^2$. Fig. 3.2 shows the sum of the pull of the leading track for each tau candidates, where the signal is clearly separated from the background. A relative accuracy of 2.7% is achieved for the signal strength measurement in the $\mu^+\mu^-H$ channel.

3.2.2.3 The hadronic channel: $qqH, H \to \tau^+\tau^-$

A cone-based τ finding algorithm has been developed. For each charged track with energy above 1.5 GeV, two cones with different open angles were made. Once the multiplicities of the smaller cone and the energy ratio between two cones satisfy a certain condition, the particles in the small cone are identified as one tau candidate. The parameters of this cone based algorithm are optimized for this measurement. Since roughly 40% of the τ lepton decays into a single charged particle and neutrino, this τ finding algorithm accepts every isolated charged particle as a τ candidate.

Two tau candidates with opposite charge are required in the objective events. This requirement has a signal efficiency of 57%, and the SM background is suppressed by

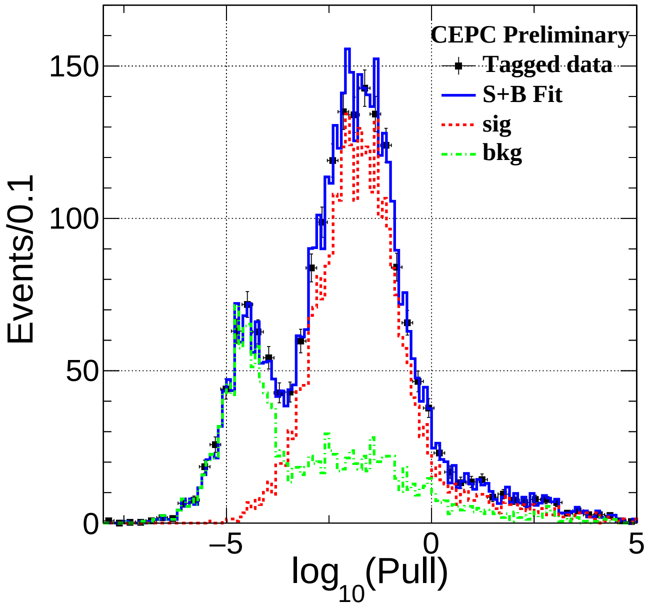

Figure 3.2: The pull of impact parameters at $Br(H \to \tau^+\tau^-)$ measurement via $\mu^+\mu^- H$ channel.

three orders of magnitudes. The remaining backgrounds include both fake signal where τ candidates arise from misidentification, for example, any leptonic decay of WW, ZZ, single W, and single Z events, and also the backgrounds with exactly the same final states:

1, Higgs background: τ candidates are generated from Higgs decay, for example $H \to WW^*/ZZ^* \to \tau^+\tau^-\nu\nu$;

2, ZH Conjugation background: Higgs decays into a pair of jets and Z decays into a pair of τ lepton;

2, ZZ backgrounds with $qq\tau\tau$ final states.

The di-jet system is defined as the remaining particles with respect to the di-tau system. Once identified, the invariant mass and recoil mass of this di-jet system is used to distinguish the ZH Conjugation and the ZZ backgrounds, see Fig. 3.4. Table. **??** shows the entire event selection of this analysis. With a signal efficiency close to 50%, the SM background is suppressed by four orders of magnitudes.

Similar as in $\mu^+\mu^- H$ channel, the track impact parameters of the τ candidate is used in the event selection. Fig. 3.3 shows the sum of the pull of the leading track for each tau candidate, where the signal is also clearly separated from the background. Applying a template fit to this pull parameter, a relative accuracy of 0.93% for the signal strength measurement is achieved for the $q\bar{q}H$ channels.

The $Br(H \to \tau^+\tau^-)$ measurement has been performed or extrapolated on the other two sub channels, both are leptonic therefore the event selections are similar to that of $\mu^+\mu^- H$ channel. For the eeH channel, the accuracy is 2.7%, slightly worse than the $\mu^+\mu^- H$ channel. For the vvH channel, though has much large statistic comparing to the $l^+l^- H$ channel, the measurement accuracy is 4.3%, mostly limited by the huge statistic

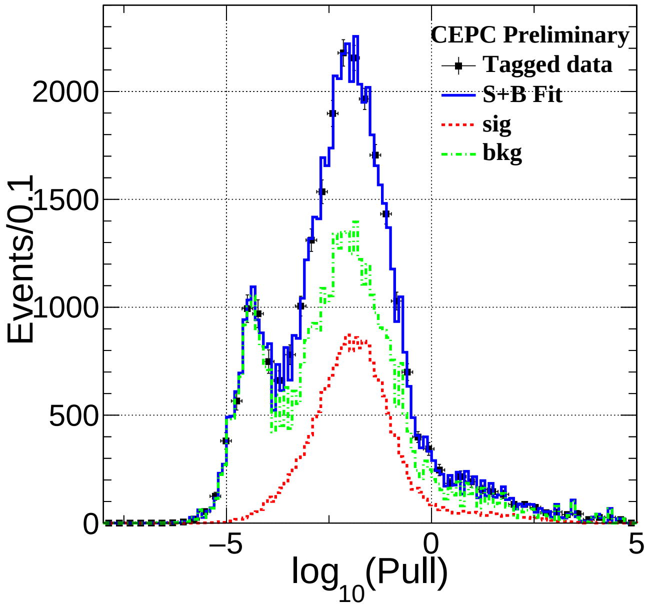

Figure 3.3: The pull of impact parameters at $Br(H \to \tau^+\tau^-)$ measurement via $q\bar{q}H$ channel.

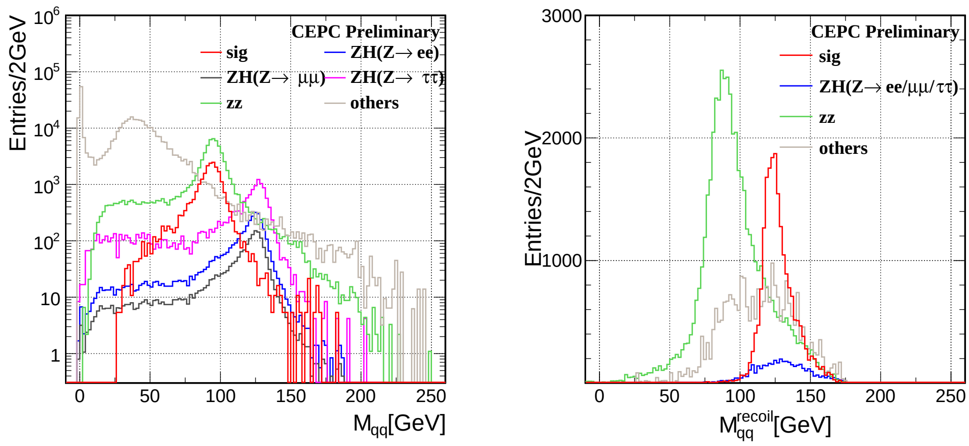

Figure 3.4: Distribution on the di-jet invariant mass and di-jet recoil mass, corresponding to line 6 and 7 in the Cut chain

of irreducible backgrounds ($WW, ZZ \to \nu\nu\tau\tau$). Therefore, a combination leads to an overall accuracy of 0.81% is achieved with the PreCDR setup.

3.2.2.4 Conclusion on the $Br(H \to \tau^+\tau^-)$ measurement

The same analyses have been re-performed with the CDR setup (APODIS detector geometry at 240 GeV center of mass energy), see Fig. **??**. The accuracies of these analyses are summarized into the second column Table 3.3. Comparing to the PreCDR setup, a slight degrading of the combined accuracy is observed in the CDR setup, which is mainly induced by the change of cross sections in the signal cross and background.

$\delta(\mu)/\mu$	PreCDR	CDR
$\mu^+\mu^-H$	2.26%	2.21%
e^+e^-H	2.72%	2.69%
$\nu\nu H$	4.29%	4.95%
qqH	0.93%	0.97%
Combined	0.81%	0.83%

Table 3.3: Signal strength measured at different sub-channels at different setups.

The Particle Flow reconstruction is vital for the $Br(H \to \tau^+\tau^-)$ measurement. In the leptonic channels, the Particle Flow oriented design precisely reconstructs the di-lepton system and determines precisely the final state particle multiplicity, which is essential for the event selection. In the qqH channel, a cone based τ finding algorithm has been developed, which could efficiently identify the tau-candidate and indicate the di-jet system. The kinematics measured from both systems efficiently control the background. As a significant fraction of the τ lepton decays into 1 prong final states, an isolated charged particle are intentionally identified as a τ candidate for both sub-channel analyses. Meanwhile, the τ candidate can be further identified from the prong charged particles using the track impact parameters, where a precise vertex system is appreciated. To summarize, the different sub-systems of the baseline detector design provides highly complementary information in these analyses, providing very clear signal signature and is extremely powerful to separate the signal from the background.

3.2.3 Differential measurements

3.2.4 Combination

3.2.5 EFT interpretation

3.3 Precision Electroweak measurements

// Please discuss with Zhijun to see what he want to put

3.3.1 R_b measurements

3.3.2 STU

3.3.3 Sterile Neutrino

3.3.4 Measurements with ISR

3.4 Flavor physics